



**HAL**  
open science

# Efficient Numerical Computations of Long-Wave Run-Up and Their Sensitivity to Grid Nesting

Fatima-Zahra Mihami, Volker Roeber, Denis Morichon

► **To cite this version:**

Fatima-Zahra Mihami, Volker Roeber, Denis Morichon. Efficient Numerical Computations of Long-Wave Run-Up and Their Sensitivity to Grid Nesting. *Water Waves*, 2022, 4 (3), pp.517-548. 10.1007/s42286-022-00070-8 . hal-04283870

**HAL Id: hal-04283870**

**<https://hal.science/hal-04283870>**

Submitted on 14 Nov 2023

**HAL** is a multi-disciplinary open access archive for the deposit and dissemination of scientific research documents, whether they are published or not. The documents may come from teaching and research institutions in France or abroad, or from public or private research centers.

L'archive ouverte pluridisciplinaire **HAL**, est destinée au dépôt et à la diffusion de documents scientifiques de niveau recherche, publiés ou non, émanant des établissements d'enseignement et de recherche français ou étrangers, des laboratoires publics ou privés.

# Efficient numerical computations of long-wave run-up and their sensitivity to grid nesting

Fatima-Zahra Mihami<sup>1</sup>, Volker Roeber<sup>1,3\*</sup>, Denis Morichon<sup>2</sup>

<sup>1</sup>Université de Pau et des Pays de l'Adour, E2S-UPPA, chair HPC-Waves, SIAME, Anglet, France

<sup>2</sup>Université de Pau et des Pays de l'Adour, E2S-UPPA, SIAME, Anglet, France

<sup>3</sup>University of Hawai'i at Mānoa, Department of Oceanography, Honolulu, HI, USA

\* volker.roeber@univ-pau.fr

---

## 1 Abstract

2 Computation of long-wave run-up has been of high interest in the fields of ocean sciences and  
3 geophysics - particularly for tsunami and river flood modeling. An accurate calculation of run-up and  
4 inundation requires the numerical model to account for a sequence of critical processes - each of them  
5 posing a different challenge to the numerical solution. This study presents the strategic development of  
6 a numerical solution technique for Shallow Water Equations with a focus on accuracy and efficiency for  
7 long-wave run-up. The present model is based on an explicit second-order Finite Volume scheme over  
8 a staggered grid that efficiently achieves fundamental properties such as well-balance and preservation  
9 of shock fronts without the need for computationally expensive solvers. The streamlined code serves  
10 as a foundation for the implementation of nested grids. Computations of commonly used long-wave  
11 benchmark tests showcase that accurate predictions of local extreme run-up can often be achieved  
12 with highly refined yet spatially focused nested grids. Strategic grid nesting can lead to stable and  
13 accurate solutions of run-up at locations of interest and reduce the computational load to a fraction of  
14 what is usually necessary for a comparable solution over a single grid.

## 15 1. Introduction

16 The estimation of run-up from long waves is crucial for the assessment and prediction of  
17 hazardous flooding scenarios associated with tsunamis and storm surges. As wave run-up is the final  
18 stage a water wave undergoes when it reaches the shore, it depends on multiple processes such as wave  
19 transformation, breaking, and interaction with dry land. Consequently, a substantial and continuous  
20 effort has been made to better understand and compute the run-up processes of long waves (Liu  
21 *et al.* (1991)). This includes studies with respect to the derivation of analytical solutions for simplified  
22 geometries (e.g., Carrier and Greenspan (1958), Synolakis (1987), Thacker (1981), Mayer and Kriebel  
23 (1995)), laboratory experiments (e.g., Hall *et al.* (1953), Briggs *et al.* (1995, 1996)), and development  
24 of new numerical methods (e.g., Liu *et al.* (1998), Titov and Synolakis (1995)). The latter provides  
25 approximate yet valid run-up solutions in more general settings suitable for the reconstruction of past  
26 events, forecasting, and practical engineering applications.

27 Numerical models for long waves, such as tides, storm surges, and tsunamis, have traditionally  
28 been based on Shallow Water Equations (SWE). Despite their simplistic hydrostatic assumptions,  
29 the SWE provide a valid basis for many long-wave problems and are often preferred over more  
30 complete equations thanks to their hyperbolic nature in which shocks can form as part of the solution.  
31 These depth-averaged equations have proven to give a reasonable balance between the accuracy and  
32 numerical cost (Brocchini and Dodd (2008)) and serve by far as the most commonly used baseline for  
33 run-up calculations (e.g., Titov *et al.* (2016), George and LeVeque (2006), Hervouet (2007)). Various  
34 numerical techniques have been proposed for the discretization of the SWE, ranging from conventional  
35 mesh-based methods such as Finite Difference (FD), Finite Volume (FV), or Finite Element (FE) to  
36 unconventional mesh-free methods such as smooth particle hydrodynamics (SPH) Wei *et al.* (2015).  
37 The numerical solutions of SWE have been subject to many trends. Earlier solutions were based  
38 on traditional FD schemes solved on a staggered grid (Arakawa and Lamb (1981)). This approach  
39 has been successfully employed in many first-generation tsunami models (e.g. TUNAMI Imamura

40 (1989), COMCOT Wang (2009)). Several wetting-drying techniques have been proposed to achieve  
41 a reasonable representation of the run-up heights. Shuto and Goto (1978) used a staggered scheme  
42 with a Lagrangian description for the moving boundaries. Another approach has been based on the  
43 Neumann-type technique, which has been used to extrapolate the velocity at the wet-dry fronts (Titov  
44 and Synolakis (1998)), while Liu *et al.* (1995) modeled the run-up based on water-level changes through  
45 flooding and drying of the cells.

46 FD methods offer a simplified solution for hyperbolic equations. However, they are known to  
47 exhibit deficiencies when dealing with flow discontinuities (Wei *et al.* (2006), Olabarrieta *et al.* (2011)),  
48 which particularly require local conservation of both mass and momentum. These conservation  
49 properties are necessary for the transport of breaking waves toward the shore and, hence, are important  
50 for the accuracy of the run-up computation. FV methods, on the other hand, solve the integral form of  
51 the SWE and directly benefit from conservation and shock-capturing capabilities. For this reason, FV  
52 methods such as Godunov (1954), and Roe (1986) solvers, which were previously used in gas dynamics,  
53 have become increasingly popular for the solution of long wave problems. A new generation of  
54 tsunami and flooding models has been developed (Berger *et al.* (2011), Macías *et al.* (2017), Dutykh  
55 *et al.* (2011), Yuan *et al.* (2020)) based on a finite volume interpretation of the equations, where the  
56 in-going and out-going fluxes over a control volume are computed with approximate Riemann solvers  
57 (e.g., Roe (1997), Harten *et al.* (1983), and Toro (1989)). These solvers are designed to preserve the  
58 hyperbolicity of the governing equations to allow for the formation of discontinuities in the numerical  
59 system. However, hyperbolicity can be a source of problems for the solution of the SWE. One drawback  
60 of this property is the well-balance between flux gradient, and source terms (Zijlema (2019)). This  
61 means that models based on the FV approach often require computationally expensive techniques to  
62 ensure the well-balance of the scheme - especially in the presence of dry cells (Wei *et al.* (2006), LeVeque  
63 (1998), Zhou *et al.* (2001), Brufau *et al.* (2002), Toro (2001), Audusse *et al.* (2015)). With respect to run-up  
64 and as a way to deal with the numerical problems of the moving shoreline, many FV schemes employ  
65 an artificial bed-wetting algorithm. These work through the definition of a minimum value of the  
66 water depth in the dry cells adjacent to the wet cells for computation of the numerical flux (Toro (2001),  
67 Dodd (1998)). Another difficulty for these schemes lies in the conservation of the non-negativity of  
68 the water depth - especially in the case of run-down (Audusse *et al.* (2004)). Nevertheless, several  
69 operational models such as FUNWAVE (Shi *et al.* (2012), COULWAVE (Kim *et al.* (2009)), and BOSZ  
70 (Roeber and Cheung (2012)) successfully utilize these schemes.

71 Another approach for solving the SWE is linked to the use of conservative staggered schemes.  
72 These methods benefit from the efficiency and robustness of the FD approximations while achieving  
73 conservative and shock-capturing properties. Such schemes have been successfully applied to flows at  
74 high Froude numbers, including hydraulic jumps and inundation of dry areas (e.g., Zhou and Stansby  
75 (1999), Stelling and Duinmeijer (2003), Madsen *et al.* (2005), Doyen and Gunawan (2014), Yamazaki *et al.*  
76 (2009)). These schemes are based on specific FD approximations, which satisfy the Rankine-Hugoniot  
77 jump condition at a discrete level (Zijlema (2019)), and achieve valid solutions for rapidly varying  
78 flows. The concept from Stelling and Duinmeijer (2003) has been widely used in many operational  
79 wave and run-up models (e.g., SWASH Zijlema *et al.* (2011), NEOWAVE Yamazaki *et al.* (2012) and  
80 Xbeach Roelvink *et al.* (2018)). This scheme guarantees the positivity of the water depth under the  
81 standard Courant-Friedrichs-Lewy (CFL) condition and therefore is very efficient for the computation  
82 of large-scale inundation problems.

83 The design of the numerical solutions of long-wave run-up requires taking the multi-scale nature  
84 of the problem into account, i.e., large-scale long-wave propagation in combination with the small-scale  
85 run-up and inundation processes. High spatial resolution is necessary for a detailed representation  
86 of the run-up process. However, computing a high-resolution grid over the entire domain is often  
87 unnecessarily expensive and can hinder the applicability of the model to real problems. With the  
88 objective of achieving efficient long-wave run-up computations, it is therefore desirable to utilize  
89 different grid sizes - each appropriate for the particular problems in the propagation and the run-up

90 stages. Different approaches have been used to obtain local mesh refinement. For example, traditional  
 91 nested grid methods have been implemented in tsunami models (Imamura (1989), Wang (2009),  
 92 Yamazaki *et al.* (2011)). These techniques are usually built into structured grids where the refinement  
 93 arises from the insertion of a sub-grid with higher resolution. The exchange of information between  
 94 the grids is achieved either with one-way or two-way interactions. On the other hand, for unstructured  
 95 grids, an adaptive mesh refinement technique has been successfully implemented in a number of  
 96 long-wave models (e.g., Berger *et al.* (2011), Sætra *et al.* (2015), Donat *et al.* (2014)). The adaptive mesh  
 97 refinement generates locally refined cells adapted to the flow condition without the need to use fixed  
 98 sub-grid Liang (2011). The refined region is, therefore, able to move with the area of interest, and  
 99 unnecessary refinement is avoided. The disadvantage of these methods lies mainly in the complexity  
 100 of the grid generation techniques, which require intensive data storage. In addition, the time step  
 101 constraint is bound to the smallest grid cell that can hinder the efficiency of the implementation for  
 102 explicit schemes (Debreu and Blayo (2008)).

103 This paper presents the rigorous development of a stable and accurate numerical framework for  
 104 the computation of long-wave run-up. We address the details of the numerical scheme and outline the  
 105 strategy for grid nesting to achieve a fast and low-cost numerical tool for run-up computations. The  
 106 verification process checks off the fundamental properties necessary for the computation of run-up:  
 107 shock-capturing capabilities, moving boundaries with bottom friction, and exchange of information  
 108 across nested grids. Two standard tsunami benchmark datasets are then employed to demonstrate the  
 109 sensitivity of long-wave run-up to the overall grid resolution as well as to the extent of the nested grid  
 110 and the refinement factor.

## 111 2. Methodology

### 112 2.1. Governing equations

113 The present study considers the two-dimensional, depth-averaged Shallow Water equations  
 114 (SWE). These equations provide a powerful baseline for long-wave modeling thanks to their wave-like  
 115 hyperbolic structure. Moreover, the SWE serve as the backbone for many numerical models that  
 116 address nearshore wave propagation and inundation. This is the case for dispersive Boussinesq-type  
 117 and non-hydrostatic models in which the governing equations contain the SWE as a subset.

118 The SWE are derived from the Navier-stokes equations under the following assumptions: (a)  
 119 the pressure is hydrostatic, and (b) the vertical distribution of the horizontal velocity is uniform (no  
 120 variation). Under these assumptions, the equations take the following differential form in Cartesian  
 121 coordinates:

$$\frac{\partial h}{\partial t} + \frac{\partial hu}{\partial x} + \frac{\partial hv}{\partial y} = 0 \quad (1)$$

$$\frac{\partial hu}{\partial t} + \frac{\partial hu^2}{\partial x} + \frac{\partial huv}{\partial y} + gh \frac{\partial \eta}{\partial x} = -gn^2 \frac{u \sqrt{u^2 + v^2}}{h^{1/3}} \quad (2)$$

$$\frac{\partial hv}{\partial t} + \frac{\partial huv}{\partial x} + \frac{\partial hv^2}{\partial y} + gh \frac{\partial \eta}{\partial y} = -gn^2 \frac{v \sqrt{u^2 + v^2}}{h^{1/3}} \quad (3)$$

122 We define  $t$  as the time variable,  $x$  and  $y$  are the space variables,  $h$  is the water depth,  $u$  and  $v$   
 123 are the depth-averaged velocities in the  $x$  and  $y$ -directions, respectively.  $\eta$  refers to the free surface  
 124 elevation:  $\eta(x, y, t) = h(x, y, t) - d(x, y)$ , where  $d$  is the positive bottom topography (1). The constant  
 125  $g$  is the gravitational acceleration and  $n$  is the Manning roughness coefficient  $[s.m^{-1/3}]$ .

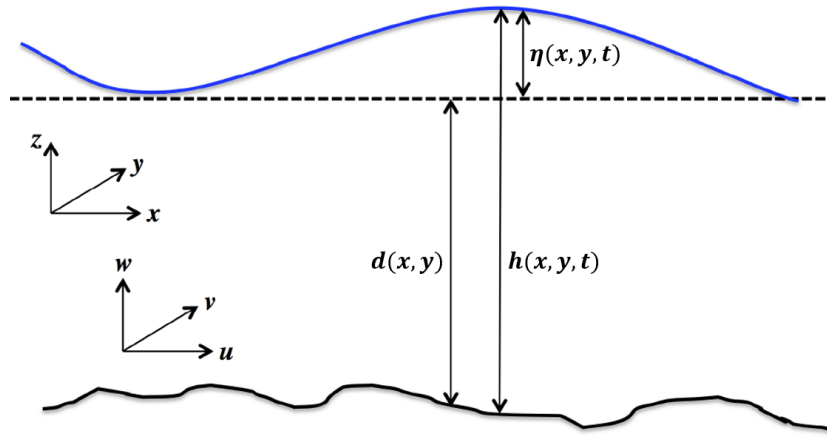


**Figure 1.** Definition sketch for the free surface flow problem with key variables.

126 We write the SWE, Eqs. 1-3 in a conservative form to ensure the conservation of mass and  
 127 momentum across discontinuities. The conserved variables, in this case, are the total water depth  $h$   
 128 and its product with the velocity components:  $hu$  and  $hv$ . In this form of the equations, we avoid the  
 129 splitting of the free surface gradient into an artificial flux gradient and a source term that includes  
 130 the effect of bed slope. This improves the well-balance properties of the numerical solution. The  
 131 preservation of shocks and discontinuities will consequently depend on the numerical approximations  
 132 of the scheme, which have to satisfy the Rankine-Hugoniot jump condition at the discrete level (Zijlema  
 133 (2019)).

134 We introduce the auxiliary variables  $p$  and  $q$ , which denote the mass fluxes:

$$p = hu \quad q = hv \quad (4)$$

135 We rewrite the SWE in the following form:

$$\frac{\partial h}{\partial t} + \frac{\partial p}{\partial x} + \frac{\partial q}{\partial y} = 0 \quad (5)$$

$$\frac{\partial hu}{\partial t} + \frac{\partial pu}{\partial x} + \frac{\partial qu}{\partial y} + gh \frac{\partial \eta}{\partial x} = -gn^2 \frac{u \sqrt{u^2 + v^2}}{h^{1/3}} \quad (6)$$

$$\frac{\partial hv}{\partial t} + \frac{\partial pv}{\partial x} + \frac{\partial qv}{\partial y} + gh \frac{\partial \eta}{\partial y} = -gn^2 \frac{v \sqrt{u^2 + v^2}}{h^{1/3}} \quad (7)$$

136 It is worth mentioning that in the momentum equations Eqs. 6 and 7, the variables  $hu$  and  $hv$  in  
 137 the local acceleration and the variables  $p$  and  $q$  in the convective acceleration play different roles. The  
 138 former is a storage quantity, while the latter is a transport quantity. Consequently, these terms are  
 139 approximated differently, and in order to avoid confusion, we avoid using the same symbols.

## 140 2.2. Conservative Staggered scheme

141 As detailed in the introduction, a variety of numerical schemes have previously been developed  
 142 for the solution of the SWE. The choice of the numerical scheme depends mainly on the problem being  
 143 addressed, which defines the requirements for the scheme properties. For the computation of long  
 144 wave run-up, a conservative shock-capturing scheme is crucial for the preservation of momentum and  
 145 propagation of shocks at the correct speed and height. Other important properties are well-balance  
 146 and non-negativity of the water depth to ensure mass conservation across wet/dry transitions without  
 147 parasitic waves. This adds to the stability and robustness of the numerical model - particularly over  
 148 irregular bathymetry. Consequently, a scheme that provides these features is suitable for computing  
 149 wave-breaking processes and, subsequently, wave run-up estimations.

150 In this study, the objective is to develop a lightweight yet accurate and stable solution structure  
 151 that keeps the computational expenses at a low level. For these reasons, we utilize a conservative  
 152 scheme on a staggered grid where the numerical fluxes are computed with simple FD approximations  
 153 instead of Riemann solvers. The SWE variables, in this case, are approximated on a staggered C-grid:  
 154 the total water depth  $h$  and the bed topography  $d$  are defined at the cell center, and the depth-averaged  
 155 velocities  $(u, v)$  are stored at the cell interfaces (see Figure. 2).

156 For the discretization, we consider a 2D rectangular computational domain with a uniform grid  
 157 spacing of  $\Delta x$  and  $\Delta y$  in the x and y directions, respectively. The variables stored at the cell center  
 158 are expressed as  $x_{i,j}$ , where  $i$  and  $j$  are the spatial indices in the x and y directions. The variables stored  
 159 at the cell interface are denoted by  $x_{i\pm\frac{1}{2},j}$  or  $x_{i,j\pm\frac{1}{2}}$  in the x- and y- directions, respectively. The time  
 160 stepping is based on discrete, non-uniform time intervals  $t^n = n\Delta t$ , where  $n$  is the time index and  $\Delta t$   
 161 is the adaptive time step. The value of each variable  $a$  at the time level  $t^n$  is denoted with  $a^n$ . The water  
 162 depth  $h$  is evaluated at each time step level  $t = n\Delta t$ , whereas, the depth-averaged velocities  $u$  and  $v$   
 163 are evaluated halfway between the present and the following time step  $t = \left(n + \frac{1}{2}\right)\Delta t$ . This leads to  
 164 the staggering of spatial and temporal information and facilitates consistent second-order accuracy in  
 165 space and time.

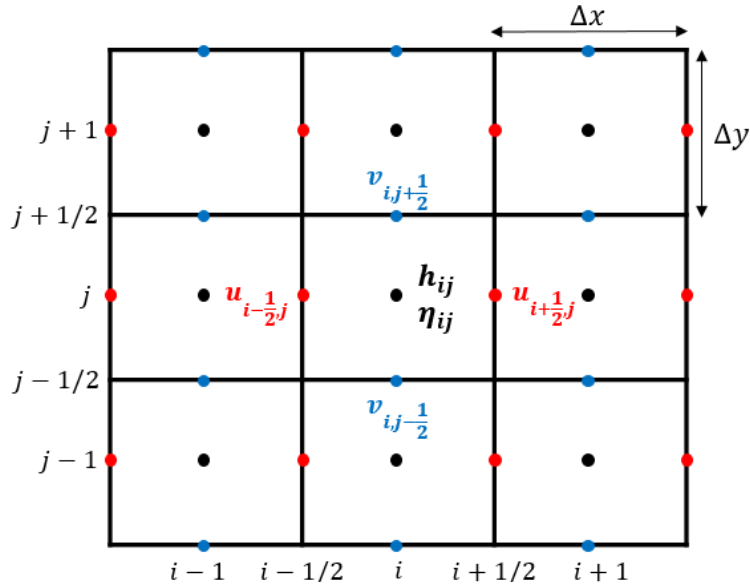


Figure 2. Schematic of the 2D staggered grid

166 The present scheme first requires the solution of the continuity equation, which is subsequently  
 167 used in the momentum equation. The discretization of the continuity equation, Eq. 5, is expressed as:

$$\frac{h_{i,j}^{n+1} - h_{i,j}^n}{\Delta t} + \frac{p_{i+\frac{1}{2},j}^n - p_{i-\frac{1}{2},j}^n}{\Delta x} + \frac{q_{i,j+\frac{1}{2}}^n - q_{i,j-\frac{1}{2}}^n}{\Delta y} = 0 \quad (8)$$

168 Where:

$$p_{i+\frac{1}{2},j}^n = \hat{h}_{i+\frac{1}{2},j}^n u_{i+\frac{1}{2},j}^{n+\frac{1}{2}} \quad q_{i,j+\frac{1}{2}}^n = \hat{h}_{i,j+\frac{1}{2}}^n v_{i,j+\frac{1}{2}}^{n+\frac{1}{2}} \quad (9)$$

169  $\hat{h}_{i\pm\frac{1}{2},j}^n$  and  $\hat{h}_{i,j\pm\frac{1}{2}}^n$  are the water depths at the cell interfaces computed with an upwind  
 170 approximation:

$$\hat{h}_{i+\frac{1}{2},j}^n = \begin{cases} h_{i,j}^n & \text{if } u_{i+\frac{1}{2},j}^{n+\frac{1}{2}} \geq 0 \\ h_{i+1,j}^n & \text{if } u_{i+\frac{1}{2},j}^{n+\frac{1}{2}} < 0 \end{cases} \quad \hat{h}_{i,j+\frac{1}{2}}^n = \begin{cases} h_{i,j}^n & \text{if } v_{i,j+\frac{1}{2}}^{n+\frac{1}{2}} \geq 0 \\ h_{i,j+1}^n & \text{if } v_{i,j+\frac{1}{2}}^{n+\frac{1}{2}} < 0 \end{cases} \quad (10)$$

171 The next step is the solution of the momentum equation, Eq. 6. First, we consider the momentum  
 172 equation without the friction term; the approximation of this term will be detailed later. We employ  
 173 the FD approximations recommended in Zijlema (2019) to achieve conservation of the momentum flux  
 174 across discontinuities, as:

$$\begin{aligned} & \frac{\bar{h}_{i+\frac{1}{2},j}^{n+1} u_{i+\frac{1}{2},j}^{n+\frac{3}{2}} - \bar{h}_{i+\frac{1}{2},j}^n u_{i+\frac{1}{2},j}^{n+\frac{1}{2}}}{\Delta t} + \frac{\hat{u}_{i+1,j}^{n+\frac{1}{2}} \bar{p}_{i+1,j}^n - \hat{u}_{i,j}^{n+\frac{1}{2}} \bar{p}_{i,j}^n}{\Delta x} + \frac{\hat{u}_{i+\frac{1}{2},j+\frac{1}{2}}^{n+\frac{1}{2}} \bar{q}_{i+\frac{1}{2},j+\frac{1}{2}}^n - \hat{u}_{i+\frac{1}{2},j-\frac{1}{2}}^{n+\frac{1}{2}} \bar{q}_{i+\frac{1}{2},j-\frac{1}{2}}^n}{\Delta y} \\ & = -g \bar{h}_{i+\frac{1}{2},j}^{n+1} \frac{\eta_{i+1,j}^{n+1} - \eta_{i,j}^{n+1}}{\Delta x} \end{aligned} \quad (11)$$

175 Regarding the free surface gradient term, the use of the updated variable  $\bar{h}_{i+\frac{1}{2},j}^{n+1}$  is necessary for the  
 176 scheme to guarantee the entropy inequality as demonstrated in Doyen and Gunawan (2014). Further,  
 177 it is necessary to approximate the convective acceleration with an upwind scheme, where the mass  
 178 fluxes  $p$  and  $q$  are the criteria for upwinding and the velocities  $u$  and  $v$  are the upwinded quantities:

$$\hat{u}_{i,j}^{n+\frac{1}{2}} = \begin{cases} u_{i-\frac{1}{2},j}^{n+\frac{1}{2}} & \text{if } \bar{p}_{i,j}^n \geq 0 \\ u_{i+\frac{1}{2},j}^{n+\frac{1}{2}} & \text{if } \bar{p}_{i,j}^n < 0 \end{cases} \quad \hat{u}_{i+\frac{1}{2},j+\frac{1}{2}}^{n+\frac{1}{2}} = \begin{cases} u_{i+\frac{1}{2},j}^{n+\frac{1}{2}} & \text{if } \bar{q}_{i+\frac{1}{2},j+\frac{1}{2}}^n \geq 0 \\ u_{i+\frac{1}{2},j+1}^{n+\frac{1}{2}} & \text{if } \bar{q}_{i+\frac{1}{2},j+\frac{1}{2}}^n < 0 \end{cases} \quad (12)$$

179 It is important to note, that a reversed approach where the upwinded quantities are  $p$  and  $q$ , leads  
 180 to errors in the computation of the momentum fluxes across discontinuities as demonstrated in Zijlema  
 181 (2019).

182 Since the mass fluxes  $p$  and  $q$  are continuous quantities, an averaged approximation of these  
 183 quantities can be applied in the computation of the convective acceleration terms:

$$\bar{p}_{i,j}^n = \frac{1}{2} (p_{i+\frac{1}{2},j}^n + p_{i-\frac{1}{2},j}^n) \quad \bar{q}_{i+\frac{1}{2},j+\frac{1}{2}}^n = \frac{1}{2} (q_{i,j+\frac{1}{2}}^n + q_{i+1,j+\frac{1}{2}}^n) \quad (13)$$

184 The flow depth, originally defined at the cell centroid, is approximated at the cell interface with  
 185 arithmetic averaging to be used in the computation of the local acceleration:

$$\bar{h}_{i+\frac{1}{2},j}^{n+1} = \frac{1}{2} (h_{i,j}^{n+1} + h_{i+1,j}^{n+1}) \quad (14)$$

186 Finally, the momentum equation, Eq. 7, in the  $y$ -direction is solved in an analogous way as:

$$\begin{aligned} & \frac{\bar{h}_{i,j+\frac{1}{2}}^{n+1} v_{i,j+\frac{1}{2}}^{n+\frac{3}{2}} - \bar{h}_{i,j+\frac{1}{2}}^n v_{i,j+\frac{1}{2}}^{n+\frac{1}{2}}}{\Delta t} + \frac{\hat{v}_{i,j+1}^{n+\frac{1}{2}} \bar{q}_{i,j+1}^n - \hat{v}_{i,j}^{n+\frac{1}{2}} \bar{q}_{i,j}^n}{\Delta y} + \frac{\hat{v}_{i+\frac{1}{2},j+\frac{1}{2}}^{n+\frac{1}{2}} \bar{p}_{i+\frac{1}{2},j+\frac{1}{2}}^n - \hat{v}_{i-\frac{1}{2},j+\frac{1}{2}}^{n+\frac{1}{2}} \bar{p}_{i-\frac{1}{2},j+\frac{1}{2}}^n}{\Delta x} \\ & = -g \bar{h}_{i,j+\frac{1}{2}}^{n+1} \frac{\eta_{i,j+1}^{n+1} - \eta_{i,j}^{n+1}}{\Delta y} \end{aligned} \quad (15)$$

187 where:

$$\vartheta_{i,j}^{n+\frac{1}{2}} = \begin{cases} v_{i,j-\frac{1}{2}}^{n+\frac{1}{2}} & \text{if } \bar{q}_{i,j}^n \geq 0 \\ v_{i,j+\frac{1}{2}}^{n+\frac{1}{2}} & \text{if } \bar{q}_{i,j}^n < 0 \end{cases} \quad \vartheta_{i+\frac{1}{2},j+\frac{1}{2}}^{n+\frac{1}{2}} = \begin{cases} v_{i,j+\frac{1}{2}}^{n+\frac{1}{2}} & \text{if } \bar{p}_{i+\frac{1}{2},j+\frac{1}{2}}^n \geq 0 \\ v_{i+1,j+\frac{1}{2}}^{n+\frac{1}{2}} & \text{if } \bar{p}_{i+\frac{1}{2},j+\frac{1}{2}}^n < 0 \end{cases} \quad (16)$$

188 and:

$$\bar{q}_{i,j}^n = \frac{1}{2} (q_{i,j+\frac{1}{2}}^n + q_{i,j-\frac{1}{2}}^n) \quad \bar{p}_{i+\frac{1}{2},j+\frac{1}{2}}^n = \frac{1}{2} (p_{i+\frac{1}{2},j+1}^n + p_{i+\frac{1}{2},j}^n) \quad (17)$$

189 The flow depth in this case is approximated as:

$$\bar{h}_{i,j+\frac{1}{2}}^{n+1} = \frac{1}{2} (h_{i,j}^{n+1} + h_{i,j+1}^{n+1}) \quad (18)$$

### 190 2.2.1. Second-order numerical accuracy

191 Staggering of the variables both in space and time and utilization of the Leapfrog scheme lead to  
 192 second-order accuracy for both the continuity and the momentum equations, except for the advection  
 193 terms, (Stelling and Duinmeijer (2003), Zijlema *et al.* (2011)). The flux terms are responsible for  
 194 transporting the conserved quantities, and consequently, the construction of the advection terms with  
 195 upwind differencing is necessary for the robustness and stability of the computed solution. However,  
 196 first-order upwind methods are diffusive, and it is, therefore, useful to target second-order accuracy  
 197 for all terms in the equations. One way to counter unnecessary numerical dissipation is based on  
 198 extending the upwind scheme to the second order in combination with a slope limiter.

199 The approximations in Eqs. 10, 12, 16, and 17 can be improved by including two neighbouring  
 200 data points instead of only one, as is the case in the first-order upwind approach. The second-order  
 201 upwind discretization is shown for Eq. 10 and applied to Eqs. 12, 16, and 17 in the same way.

$$\hat{h}_{i+\frac{1}{2},j}^n = \begin{cases} h_{i,j}^n + \frac{1}{2}\psi\left(r_{i+\frac{1}{2},j}^+\right)\left(h_{i,j}^n - h_{i-1,j}^n\right), & \text{if } u_{i+\frac{1}{2},j}^n \geq 0 \\ h_{i+1,j}^n + \frac{1}{2}\psi\left(r_{i+\frac{1}{2},j}^-\right)\left(h_{i+1,j}^n - h_{i+2,j}^n\right), & \text{if } u_{i+\frac{1}{2},j}^n < 0 \end{cases} \quad (19)$$

202  $r_{i+\frac{1}{2},j}^+$  and  $r_{i+\frac{1}{2},j}^-$  are respectively the left and right gradients of the flow depth:

$$r_{i+\frac{1}{2},j}^+ = \frac{h_{i+1,j}^n - h_{i,j}^n}{h_{i,j}^n - h_{i-1,j}^n}, \quad r_{i+\frac{1}{2},j}^- = \frac{h_{i+1,j}^n - h_{i,j}^n}{h_{i+2,j}^n - h_{i+1,j}^n} \quad (20)$$

203  $\psi(r)$  is the slope limiter function, which locally reduces the solution from second to first order.  
 204 This is often necessary at locations with opposite slopes, zero gradients, or sharp transitions. Here, a  
 205 Generalized MinMod slope limiter is used :

$$\phi(r, \theta) = \max\left(0, \min\left(\theta r, \frac{1+r}{2}, \theta\right)\right) \quad (21)$$

206  $\theta$  is a parameter that controls the diffusivity. The generalized MinMod limiter is most dissipative  
 207 for  $\theta = 1$  when it reduces to the traditional MinMod limiter, and it is least diffusive for  $\theta = 2$ .

208 A predictor-corrector method can be used to improve the temporal accuracy of the advection  
 209 terms to retain second-order accuracy in time. Here, we employ the Total Variation Diminishing (TVD)  
 210 Runge-Kutta method. This method enhances the accuracy of the scheme in time while maintaining  
 211 the strong stability property of the first-order Euler integration (Gottlieb *et al.* (2001)). It is worth  
 212 mentioning that other time integration methods can be combined with the above-described spatial



213 discretization. For example, [Zijlema et al. \(2011\)](#) used a MacCormack approach for the second-order  
214 integration in time.

215 We split the SWE equations into a convective acceleration term  $\mathcal{F}$  and a free surface gradient  
216 term  $\mathcal{G}$ , which simplifies the description of the multi-step method:

$$\frac{\partial U}{\partial t} + \mathcal{F}(U) + \mathcal{G}(U) = 0 \quad (22)$$

Where:

$$U = \begin{bmatrix} h \\ hu \\ hv \end{bmatrix} \quad \mathcal{F}(U) = \begin{bmatrix} \frac{\partial p}{\partial x} + \frac{\partial q}{\partial y} \\ \frac{\partial pu}{\partial x} + \frac{\partial qu}{\partial y} \\ \frac{\partial pv}{\partial x} + \frac{\partial qv}{\partial y} \end{bmatrix} \quad \mathcal{G}(U) = \begin{bmatrix} 0 \\ gh \frac{\partial \eta}{\partial x} \\ gh \frac{\partial \eta}{\partial y} \end{bmatrix} \quad (23)$$

217 The discretization described in Eqs. 8, 11, and 15 can be summarized in the following expression:

$$U_{ij}^{n+1} = U_{ij}^n - \Delta t \mathcal{F}(U_{ij}^n) - \Delta t \mathcal{G}(U_{ij}^{n+1}) \quad (24)$$

218 Where

$$U_{ij}^n = \begin{bmatrix} h_{ij}^n \\ \bar{h}_{i+\frac{1}{2},j}^n u_{i+\frac{1}{2},j}^{n+\frac{1}{2}} \\ \bar{h}_{i,j+\frac{1}{2}}^n v_{i,j+\frac{1}{2}}^{n+\frac{1}{2}} \end{bmatrix} \quad (25)$$

219 At each time step, the variables  $(h, hu, hv)$  are solved using a two-stage time integration with an  
220 intermediate solution obtained by the predictor step. In the first step, we solve the equations with only  
221 the advection terms on the right-hand side:

$$U_{ij}^* = U_{ij}^n - \Delta t \mathcal{F}(U_{ij}^n) \quad (26)$$

222 This leads to a predictor solution of first-order accuracy for the complete continuity equation  
223 and incomplete momentum equations due to the lack of source terms. In the second step, the surface  
224 gradient terms are added to the momentum equations, and the predicted variables are corrected to full  
225 second-order accuracy in time by:

$$U_{ij}^{n+1} = \frac{\Delta t}{2} (U_{ij}^n + U_{ij}^*) - \frac{\Delta t}{2} \mathcal{F}(U_{ij}^*) - \Delta t \mathcal{G}(U_{ij}^{n+1}) \quad (27)$$

226 It is important to emphasize that the predictor step of the time integration should only involve  
227 the convective acceleration terms. The source terms attain second-order accuracy by staggering the  
228 flow speed variables in time, and an application of Eq. 26 to the source terms would lead to inaccurate  
229 results.

230 The last term on the right-hand side of Eq. 27 applies only to the momentum equations and  
231 involves the corrected flow depth value  $h^{n+1}$ . This completes the fully explicit time integration where  
232 no system of equations with data dependencies has to be solved.

### 233 2.2.2. Flooding and drying

234 The wetting and drying process requires the model's performance for two fundamental processes.  
235 The well-balance and the preservation of positivity of the water depth across wet/dry boundaries.

236 An explicit time integration is bound to the Courant–Friedrichs–Lewy (CFL) condition given by:

$$\left[ \frac{\max\left(u_{i+\frac{1}{2},j}^{n+\frac{1}{2}}, 0\right) - \min\left(u_{i-\frac{1}{2},j}^{n+\frac{1}{2}}, 0\right)}{\Delta x} + \frac{\max\left(v_{i,j+\frac{1}{2}}^{n+\frac{1}{2}}, 0\right) - \min\left(v_{i,j-\frac{1}{2}}^{n+\frac{1}{2}}, 0\right)}{\Delta y} \right] \Delta t \leq 1 \quad (28)$$

237 Under this condition, the scheme preserves the non-negativity of the water depth (Zijlema (2019),  
 238 Gunawan (2015)). This has the advantage that the run-up and inundation limits are inherent solutions  
 239 of the numerical scheme and are not subject to additional ad-hoc flooding and drying treatments or  
 240 require particular restructuring of the flux and source terms.

241 The time step that satisfies Eq. 28 is computed in dependence of the Courant number  $Cr \leq 1$ , grid  
 242 spacing, and maximum flow speed as:

$$\Delta t = \frac{Cr}{\max\left(\frac{|u_{i+\frac{1}{2},j}^{n+\frac{1}{2}}| + \sqrt{g\hat{h}_{i+\frac{1}{2},j}^n}}{\Delta x}, \frac{|v_{i,j+\frac{1}{2}}^{n+\frac{1}{2}}| + \sqrt{g\hat{h}_{i,j+\frac{1}{2}}^n}}{\Delta y}\right)} \quad (29)$$

243 Since the flow depth can become arbitrarily small at the wet-dry transitions and, therefore, can  
 244 lead to excessively high-velocity values, it makes sense to limit the minimum flow depth at the run-up  
 245 front to a physically and numerically meaningful level. For efficiency reasons, the velocity values can  
 246 be set to zero when the local water level falls below a threshold value  $h_{min}$ , and the calculation of the  
 247 momentum equations can be skipped.

$$u_{i+\frac{1}{2},j}^{n+\frac{3}{2}} = 0 \quad \text{if} \quad \frac{h_{i,j}^{n+1} + h_{i+1,j}^{n+1}}{2} < h_{min} \quad (30)$$

$$v_{i,j+\frac{1}{2}}^{n+\frac{3}{2}} = 0 \quad \text{if} \quad \frac{h_{i,j}^{n+1} + h_{i,j+1}^{n+1}}{2} < h_{min} \quad (31)$$

248 The value of  $h_{min}$  should be chosen as small as possible to accurately resolve the wet-dry front  
 249 (Toro (2001)), but large enough to avoid physically questionable values in the local flow speed, which  
 250 can cause excessively small time steps as shown in Eq. 29. It should be noted that the present scheme  
 251 is not particularly sensitive to this threshold, and values between  $10^{-8}$  and  $10^{-4}$  m lead to virtually  
 252 identical results. For the sake of quality verification and validation, we are using  $h_{min} = 10^{-8}$  m in the  
 253 subsequent examples.

### 254 2.2.3. Friction term

255 The friction terms added to the momentum equations are discretized as:

$$gn^2 \frac{u_{i+\frac{1}{2},j}^{n+\frac{3}{2}} \sqrt{\left(u_{i+\frac{1}{2},j}^{n+\frac{1}{2}}\right)^2 + \left(\bar{v}_{i+\frac{1}{2},j}^{n+\frac{1}{2}}\right)^2}}{\left(\bar{h}_{i+\frac{1}{2},j}^{n+1}\right)^{1/3}} \quad \text{and} \quad gn^2 \frac{v_{i,j+\frac{1}{2}}^{n+\frac{3}{2}} \sqrt{\left(\bar{u}_{i,j+\frac{1}{2}}^{n+\frac{1}{2}}\right)^2 + \left(v_{i,j+\frac{1}{2}}^{n+\frac{1}{2}}\right)^2}}{\left(\bar{h}_{i,j+\frac{1}{2}}^{n+1}\right)^{1/3}} \quad (32)$$

256 Where:

$$\begin{aligned} \bar{v}_{i+\frac{1}{2},j}^{n+\frac{1}{2}} &= \frac{1}{4} \left( v_{i,j-\frac{1}{2}}^{n+\frac{1}{2}} + v_{i,j+\frac{1}{2}}^{n+\frac{1}{2}} + v_{i+1,j-\frac{1}{2}}^{n+\frac{1}{2}} + v_{i+1,j+\frac{1}{2}}^{n+\frac{1}{2}} \right) \\ \bar{u}_{i,j+\frac{1}{2}}^{n+\frac{1}{2}} &= \frac{1}{4} \left( u_{i-\frac{1}{2},j}^{n+\frac{1}{2}} + u_{i+\frac{1}{2},j}^{n+\frac{1}{2}} + u_{i-\frac{1}{2},j+1}^{n+\frac{1}{2}} + u_{i+\frac{1}{2},j+1}^{n+\frac{1}{2}} \right) \end{aligned} \quad (33)$$

257 and  $n$ , with units [ $sm^{-1/3}$ ], is the Manning roughness coefficient representing the bottom property.  
 258 Using the variables  $\left(h_{i,j+\frac{1}{2}}^{n+1}, u_{i+\frac{1}{2},j}^{n+\frac{3}{2}}, v_{i+\frac{1}{2},j}^{n+\frac{1}{2}}\right)$  from the next time step in the friction terms improves the  
 259 accuracy and the robustness of the solution (Zijlema *et al.* (2011)).

260 Some of the following numerical tests, presented in section 3, are computed with the  
 261 Darcy-Weisbach formulation, which requires replacement of the term  $\frac{gn^2}{h^{1/3}}$  by  $\frac{f}{8}$ .  $f$  is the dimensionless  
 262 Darcy-Weisbach coefficient.

### 263 2.3. Nested grid method

264 The accuracy and applicability of a numerical model for free surface flows can substantially  
 265 benefit from an efficient mesh refinement technique. Here, we concentrate on the nested grid method,  
 266 which provides a reasonable trade-off between computational complexity and the gain in accuracy of  
 267 the numerical solution for long wave run-up. A simplified approach for mesh refinement involves  
 268 the insertion of a high-resolution Child grid into a surrounding Parent grid of coarser resolution. The  
 269 grids are herein fixed in space and predefined before the computation is executed. The SWE are solved  
 270 independently in each grid. Consequently, the overall solution structure of the governing equations  
 271 remains untouched as the exchange between the grids only requires interpolation of the key variables.

272 The staggered C-grid has been widely used in combination with embedded grid models due to  
 273 its simplicity and conservative properties (Debreu and Blayo (2008), Liu *et al.* (1995), Herzfeld and  
 274 Rizwi (2019)). In this study, we build the nested grid approach on some of the techniques used and  
 275 validated by several previously developed tsunami models (Imamura (1989), Wang (2009)). Several  
 276 performances are expected from a functioning grid nesting technique:

277 **Data exchange:** The exchange of information between the grids occurs along the boundary of the  
 278 inner grid. The Parent grid provides the boundary conditions to the Child grid in a one-way interaction.  
 279 The flux variables (i.e.,  $hu$  and  $hv$ ) from the coarse grid are linearly interpolated in time and space and  
 280 then dynamically imposed in each time step as boundary conditions to the solution of the Child grid  
 281 (See Figure. 3). For a two-way interaction, the high-resolution free-surface elevation from the Child  
 282 grid is used to update the information in the Parent grid via an averaging operator. The update of the  
 283 free-surface only occurs inside the feedback interface in the Parent grid (See Figure. 3), rather than  
 284 in the domain occupied by the Child grid. Several authors have proposed separating the feedback  
 285 interface from the dynamic interface where the boundary values are interpolated (Phillips and Shukla  
 286 (1973), Zhang *et al.* (1986), Oey and Chen (1992)). This separation helps to avoid inconsistencies between  
 287 the solutions and stability problems that often arise from forcing the solution of the Parent grid with  
 288 the updated values of the inner grid (Debreu and Blayo (2008)).

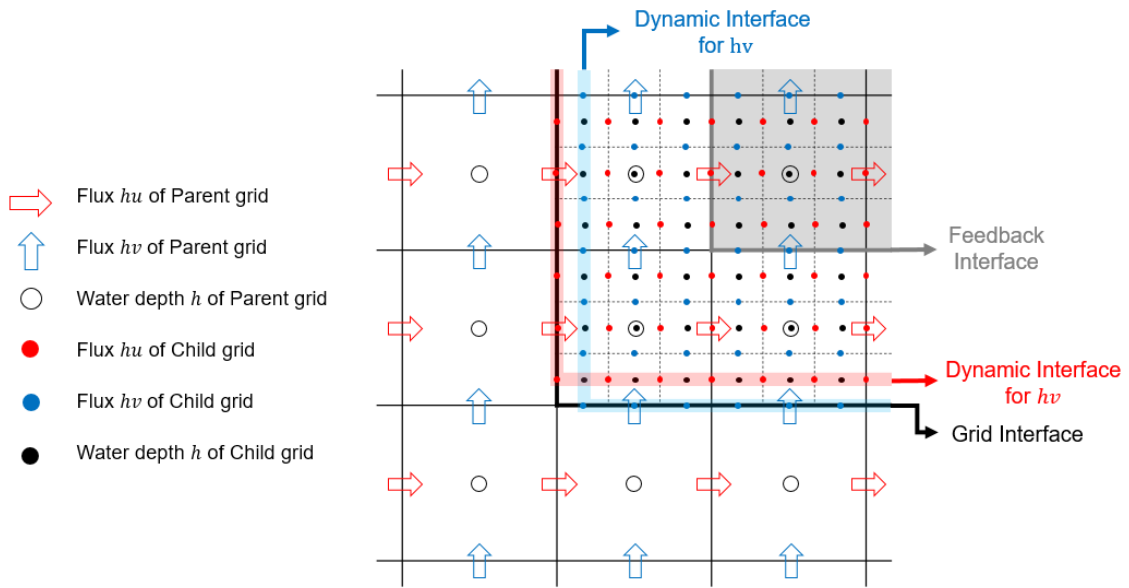


Figure 3. Schematic illustrating the two-way nesting process on a Arakawa C grid

289 **Time synchronization** : The use of an explicit time integration means that the model needs to  
 290 verify the CFL stability condition, and the ratio  $\Delta t/\Delta x$  must be kept smaller than a given value on  
 291 the whole grid hierarchy. Consequently, a temporal refinement must be applied in addition to the  
 292 spatial mesh refinement. The integration algorithm for a time refinement of 3 is depicted in Figure. 4.  
 293 The model is first integrated on the Parent grid  $\Omega_p$  with a time step equal to  $\Delta t_{p1}$ , the model is then  
 294 advanced multiple times on the Child grid  $\Omega_c$  to reach the same physical time as the outer grid. To  
 295 synchronize the two solutions, the last time step in the inner grid is imposed:  $\Delta t_{c3} = \Delta t_{p1} - \sum \Delta t_{ci}$ .

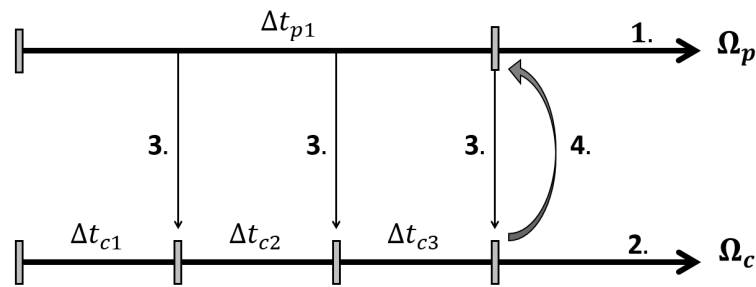


Figure 4. Schematic illustrating the two-way nesting process

- 296 • 1 : Model integration on the Parent grid  $\Omega_p$
- 297 • 2 : Model integration on the Child grid  $\Omega_c$
- 298 • 3 : Time and space interpolation of the boundary values
- 299 • 4 : Update of the Parent Grid in feedback domain

### 300 3. Verification

301 A systematical analysis of a numerical solution for long-wave run-up requires benchmarking.  
 302 Since the model was developed from scratch and involves a combination of adapted numerical features,  
 303 it is required to first verify its performance for idealized flow problems, for which analytical solutions

304 have been derived. These tests examine the model's ability to handle important flow processes, such  
 305 as flow discontinuities and wet/dry transitions. These features are particularly critical for the quality  
 306 of the computed run-up and can often pose numerical challenges. The implementation of the nested  
 307 grid approach is then verified with a 2D moving boundaries problem.

### 308 3.1. Shock-capturing capabilities

309 Shock-capturing schemes refer to numerical methods that can directly solve wave propagation  
 310 with large gradients and rapid changes in the free-surface and velocity regimes. Such nonlinear  
 311 phenomena are present in many wave problems (e.g., wave breaking, dam-break wave propagation,  
 312 and propagation of wet/dry fronts). Consequently, a lot of effort is made to compute shock waves as  
 313 part of the complete solution (Toro (2001)). A stable numerical solution for shock waves targets the  
 314 generation and propagation of an oscillation-free discontinuity without excessive smearing across the  
 315 shock front.

316 In the following, we examine the solution of the present model in handling discontinuities  
 317 and assess the accuracy and quality of the results. Since many shock-capturing flow models are  
 318 built around Riemann solvers, we compare the solution from the presented scheme, referred to as  
 319 "Present Scheme", with the solution obtained by a 1D HLLC Riemann solver ("HLLC Scheme"). The  
 320 HLLC scheme used for comparison was coded based on the techniques given by Toro (2001). For  
 321 consistency with the presented scheme, the first-order HLLC scheme is extended to second-order  
 322 accuracy through a MUSCL reconstruction (Van Leer (1979)) combined with a generalized MinMod  
 323 limiter and a predictor-corrector Runge-Kutta time integration.

The dambreak problem is a widely used test to demonstrate the shock-capturing capabilities of  
 numerical schemes. We consider a one-dimensional dambreak over a wet bed of uniform depth. The  
 domain is 1 m long and the initial condition is:

$$h(x, 0) = \begin{cases} 1 \text{ m} & \text{if } x \leq 0.5 \text{ m} \\ 0.2 \text{ m} & \text{otherwise} \end{cases} \quad u(x, 0) = 0 \text{ m/s}$$

324 The analytical solution for this test was derived by Stoker (1957) and consists of a shock and a  
 325 rarefaction wave moving in opposite directions from the center of the domain. The solutions of the  
 326 dambreak test for 100 grid cells ( $\Delta x = 1 \text{ cm}$ ) and at  $t = 0.1 \text{ sec}$  are shown in Figure. 5. For both schemes,  
 327 we use a constant Courant number of  $CN = 0.7$  and a diffusion parameter in the generalized MinMod  
 328 limiter  $\theta = 1.5$ .

329 Both numerical schemes correctly capture the rarefaction and shock waves despite small  
 330 discrepancies in comparison to the analytical solution. This small mismatch can be reduced significantly  
 331 with a reduction in grid size. In general, the Present scheme achieves slightly sharper solutions around  
 332 the flow transitions compared to the HLLC scheme. Consequently, the Present scheme contains  
 333 smaller L1-norm errors than the HLLC scheme, as listed in Table 1, albeit the fact that both solutions  
 334 converge towards the exact solution with mesh refinement. The presented model is able to compute the  
 335 propagation of shocks with the correct wave speed and height, proving its powerful shock-capturing  
 336 capability without the need for the computationally expensive sampling of the solution as it is necessary  
 337 for the HLLC scheme.

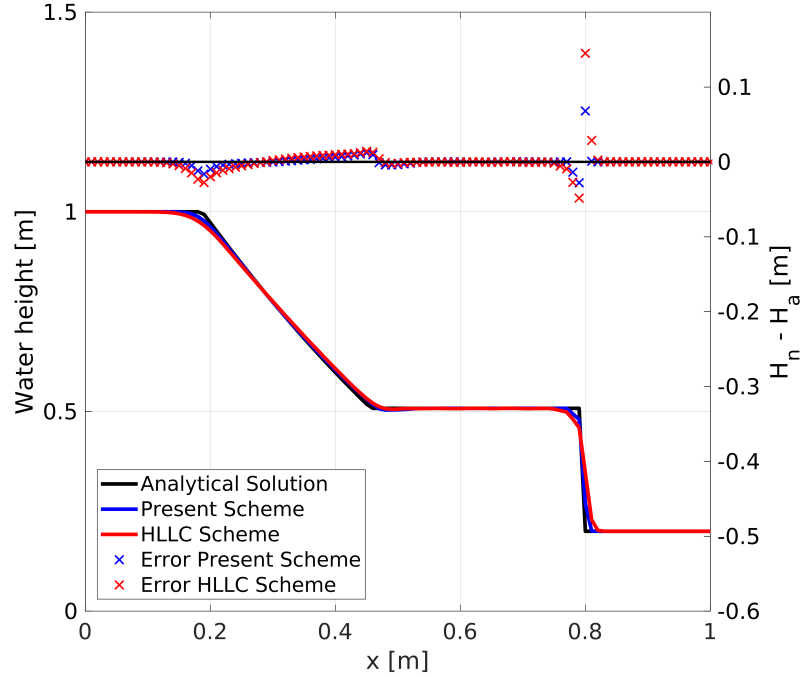


**Figure 5.** Dambreak over wet bed: Water height profiles from the Present and HLLC schemes at  $t = 0.1$  sec for a cell size  $\Delta x$  of 1 cm.

Number of cells	$h$		$hu$	
	Present	HLLC	Present	HLLC
100	$3.69 \times 10^{-3}$	$5.20 \times 10^{-3}$	$6.37 \times 10^{-3}$	$1.24 \times 10^{-2}$
200	$1.85 \times 10^{-3}$	$2.56 \times 10^{-3}$	$3.17 \times 10^{-3}$	$6.22 \times 10^{-3}$
400	$7.90 \times 10^{-4}$	$1.29 \times 10^{-3}$	$1.90 \times 10^{-3}$	$3.22 \times 10^{-3}$
800	$4.44 \times 10^{-4}$	$6.36 \times 10^{-4}$	$7.76 \times 10^{-4}$	$1.52 \times 10^{-3}$

**Table 1.** Dambreak over a wet bed: L1-norm error

### 338 3.2. Moving boundaries

339 An essential feature of shallow water models used for flood and inundation mapping is the ability  
 340 to compute wet-dry transitions and track moving boundaries. The biggest challenges are associated  
 341 with the definition of the numerical fluxes and source terms in the presence of dry cells. A clean and  
 342 stable representation of the moving boundary is essential for the correct description of run-up and  
 343 inundation limits independent of the previous stages of wave propagation and breaking.

344 We investigate the performance of the present model in describing fast sheet flows induced by a  
 345 dambreak over a dry bed with and without frictional resistance. This test is also used to verify the  
 346 implementation of the friction term.

347 The test case involves a 2000 m long horizontal channel of uniform depth with  $\Delta x = 5$  m grid  
 348 spacing and the following initial condition:

$$h(x, 0) = \begin{cases} 6 \text{ m} & \text{if } x \leq 1000 \text{ m} \\ 0 \text{ m} & \text{otherwise} \end{cases} \quad u(x, 0) = 0 \text{ m}$$

349 The test is computed with a minimum water depth of  $h_{min} = 10^{-8}$  m and a Courant number of 0.7.  
 350 Two cases are taken into account:

- 351 1. **Dambreak without friction.** The numerical results are compared with the Ritter solution. The  
 352 solution involves a wet-dry front propagating downstream and a rarefaction wave moving  
 353 upstream into the reservoir.
- 354 2. **Dambreak with friction.** In this case, the Darcy-Weisbach friction law with a coefficient  $f =$   
 355  $8g/40^2$  is utilized in the friction source term of the momentum equations. The reference solution  
 356 is based on the Dressler/Whitham/Chanson conceptual model (Dressler (1952), Whitham (1955),  
 357 Chanson (2009)), which is based on the assumption that near the wavefront, frictional resistance  
 358 controls the fluid motion. The exact shape of the wavefront can be found in Chanson (2009). In  
 359 contrast to the process at the downstream wave, the frictional resistance in the rarefaction regime  
 360 is neglected, and the solution at the front can be described by a modified Ritter's solution as  
 361 presented in Delestre *et al.* (2013).

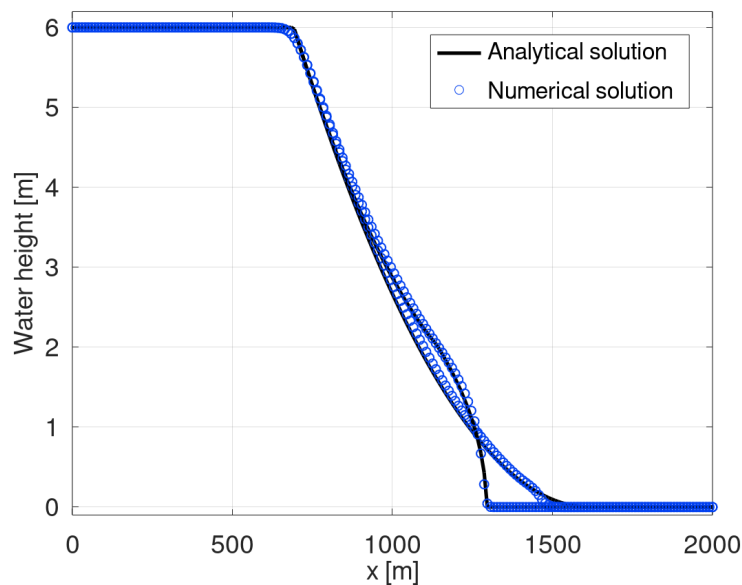


**Figure 6.** Dambreak on dry bed: Water height profiles after  $t = 40$  sec for grid spacing  $\Delta x = 10$  m. The wave front around 1250 m corresponds to the solution with a friction coefficient of  $f = 8g/40^2$ .

362 In both cases, good agreement between the reference and the numerical solutions is obtained  
 363 (Fig. 6). In the case of bottom friction, the model accurately captures the deceleration of the wavefront,  
 364 which verifies its capability of correctly handling bottom roughness. As before, the results can be  
 365 improved through mesh refinement but not through further reduction of the predefined minimum  
 366 water depth  $h_{min}$ .

### 367 3.3. Nested grid implementation

368 In this section, we examine the accuracy of the nested grid implementation. This step is important  
 369 to scrutinize the model performance with respect to the information exchange across different grid  
 370 resolutions, especially in the presence of wet/dry transitions. For applications related to long-wave  
 371 run-up, the nested grid approach is expected to deal with moving boundaries and fast flows over  
 372 varying topography in two-dimensional settings. A few analytical solutions of the SWE exist for  
 373 problems in the 2D horizontal plane. The oscillation in a parabolic basin is one of them, as it addresses  
 374 a two-dimensional run-up problem, which helps examine the validity of the numerical structure in the  
 375 combined  $xy$ -directions.

376 The water oscillation is induced inside a  $[0, L] \times [0, L]$  parabolic basin given by:

$$z(r) = -h_0 \left(1 - \frac{r^2}{a^2}\right) \quad \text{where} \quad r = \sqrt{\left(x - \frac{L}{2}\right)^2 + \left(y - \frac{L}{2}\right)^2}$$

377 The value of  $h_0$  represents the still water depth at the basin center, and  $a$  is the radius of the wetted  
 378 perimeter. The exact solution for this test was derived by [Thacker \(1981\)](#). For a smooth bed with no  
 379 friction, the analytical solution for the water depth is described as:

$$h(r, t) = h_0 \left( \frac{\sqrt{1 - A^2}}{1 - A \cos(\omega t)} - 1 - \frac{r^2}{a^2} \left( \frac{1 - A^2}{(1 - A \cos(\omega t))^2} - 1 \right) \right) - z(r)$$

380 where  $\omega = \sqrt{8gh_0/a}$  is the frequency of the oscillation, and the coefficient  $A =$   
 381  $(a^2 - r_0^2) / (a^2 + r_0^2)$  with  $r_0$  the radius of the initial shoreline. For the setup of the dimensions of  
 382 the parabola and the initial condition of the free surface, we use  $a=1$  m,  $r_0 = 0.8$  m,  $h_0 = 0.1$  m and  $L$   
 383  $=4$  m.

384 The analytical solution is used to verify the symmetry and accuracy of the nested grid  
 385 implementation. Here, we place a nested domain off-center, including the moving waterline, with a  
 386 refinement factor of 4. The use of an off-center nested grid is critical to verifying the grid exchange for  
 387 both the normal and cross fluxes. The Parent grid is computed with a quadratic cell size of 2 cm by  
 388 2 cm. The inner Child grid is computed with  $\Delta x = \Delta y = 0.5$  cm.

389 The water height evolution at the center of the basin is shown in [Fig. 7](#) after 40 sec corresponding  
 390 to over 17 full cycles in the Parent grid. The present solution convinces through the maintenance of  
 391 amplitude and phase over multiple oscillation cycles the quality of the second-order numerical scheme.  
 392 These results confirm not only the low numerical diffusion but also the smooth transition across the  
 393 wet/dry boundary inherent to the model without the need for excessively small grid sizes.

394 [Fig. 8](#) depicts the free surface transect across the basin center line at several stages,  $t = T$ ,  
 395  $t = T + T/4$ , and  $t = T + T/2$ , where  $T = 2\pi/\omega$  denotes the oscillation period. The run-up is well  
 396 described, and no numerical artifact arises from the exchange between the Parent and Child grid. In  
 397 addition, [Fig. 9](#) gives a visual impression of the three-dimensional problem and showcases that the  
 398 definition of the run-up outline benefits from mesh refinement.

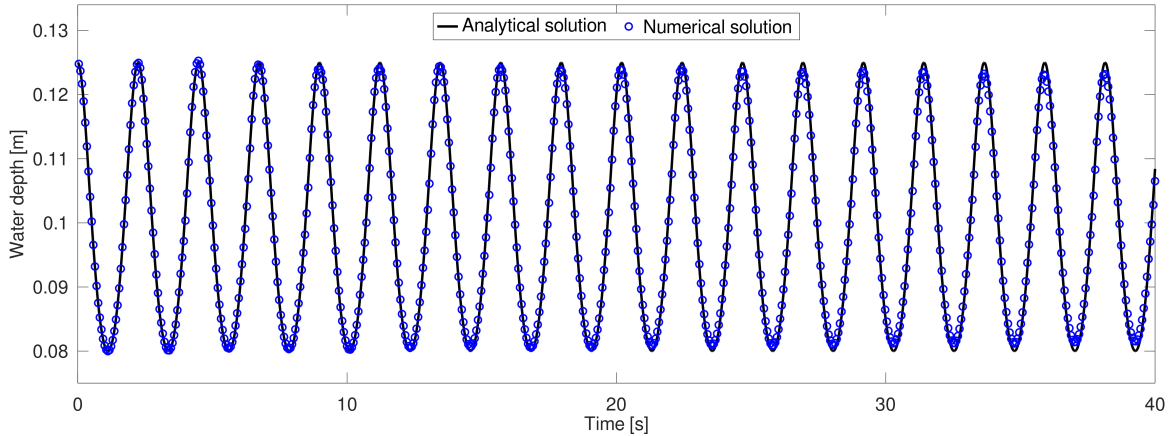


**Figure 7.** Time series of water height at center point of parabolic basin ( $x = L/2, y = L/2$ ). Grid spacing  $\Delta x = \Delta y = 2$  cm. The numerical solution is of low diffusion without requiring excessively fine mesh sizes.



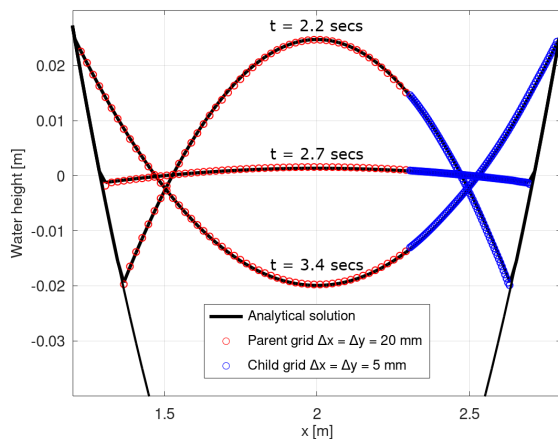


**Figure 8.** Oscillation in a parabolic basin: Cross-section of water height after one full oscillation. Each circle represents the solution from the numerical model at each grid cell across the transect. The solution from the nested grid is indicated with blue circles.

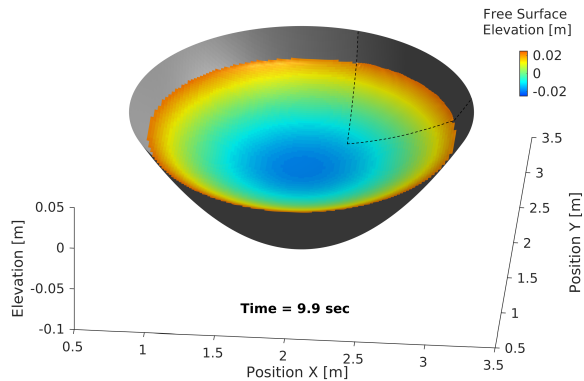


**Figure 9.** Free surface elevation of oscillation in parabolic basin with grid nesting after 4.5 cycles (9.9 sec). The refined Child grid is denoted by the dashed line and shows a more detailed run-up limit than the coarse Parent grid.

#### 399 4. Effect of grid nesting on wave run-up

400 Previous verification efforts have ensured that the present model correctly handles the  
 401 fundamental features that are essential for the accurate computation of long-wave run-up. The  
 402 following tests examine the sensitivity of the computed results to grid nesting for efficient computation  
 403 of local run-up problems. For this purpose, we utilize two standard experimental benchmark tests  
 404 that have been widely used in the tsunami community and that highlight the complexity of the local  
 405 long-wave run-up. The two tests present common long-wave features such as the increase in local  
 406 wave run-up from the collision of two or more waves as well as extreme run-up over highly detailed  
 407 terrain. We will present an analysis of the sensitivity of the computed run-up to the general mesh size  
 408 and further investigate the sensitivity of the maximum run-up extent to the size of the nested grid and  
 409 the refinement factor.

##### 410 4.1. Solitary wave run-up around a conical island

411 The transformation of long waves around islands has attracted a lot of attention in the past -  
 412 especially among tsunami researchers. A common observation is that long waves can refract and  
 413 diffract around an island from both sides and collide in the back. In some cases, the maximum  
 414 run-up occurs counter-intuitively at the island's lee side due to a superposition effect when the  
 415 refracted/diffracted waves from both sides run into each other and double up. The problem of the  
 416 conical island is exemplary since the high run-up and inundation at the lee side cannot be approximated  
 417 with empirical formulae or computationally cheap 1D calculations. Instead, the problems require a full  
 418 2D solution that naturally exhibits a substantial computational effort.

419 [Briggs et al. \(1995\)](#) conducted a large-scale laboratory experiment to investigate solitary wave  
 420 transformation around a conical island. The basin is 25 m by 30 m with a circular island in the shape of  
 421 a truncated cone constructed of concrete with a diameter of 7.2 m at the bottom and 2.2 m at the top.  
 422 The island is 0.625 m high and has a side slope of 1:4. A 27.4-m long directional wavemaker consisting  
 423 of 61 paddles generated the input solitary waves for three laboratory tests. Wave absorbers at the three  
 424 remaining sidewalls reduced reflection in the basin. Further details about the laboratory model setup,  
 425 the location of the wave gauges, and the numerical setup can be found in [NTHMP \(2012\)](#).

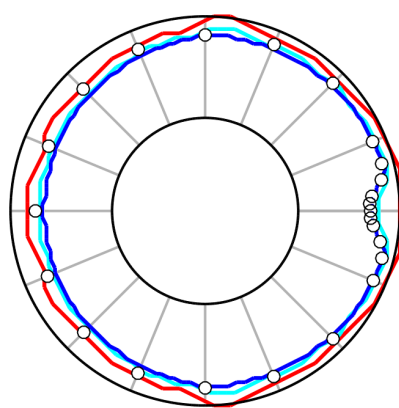
426 The present study focuses on experiments with a water depth  $h = 0.32m$  and solitary wave  
 427 heights of  $A/h = 0.1$ . Consistent with NTHMP benchmark problem 6 ([NTHMP \(2012\)](#)), our numerical

428 test uses the measured wave heights of  $A/h = 0.096$  from the laboratory experiment instead of the  
429 target wave heights as they better represent the recorded data and thus the incident wave conditions to  
430 the conical island. A reflective boundary condition is imposed at the lateral sides. The wave absorbers  
431 from the laboratory layout are not considered since their absorbing performance is unknown. The  
432 model is set up with a reference grid of  $\Delta x = \Delta y = 5$  cm. A Manning roughness coefficient of  $n = 0.012$   
433  $s/m^{1/3}$  accounts for the smooth concrete finish according to [Chaudhry \(2007\)](#). The Courant number  
434 is set to  $Cr = 0.5$ . The model setup is comparable to earlier work and will be used as a reference as  
435 it is expected to return solutions of similar and comparable quality to previously published studies.  
436 The results from the free surface elevation observed at five wave gauges are omitted here as they are  
437 comparable to previously published results.

#### 438 **Sensitivity to grid resolution:**

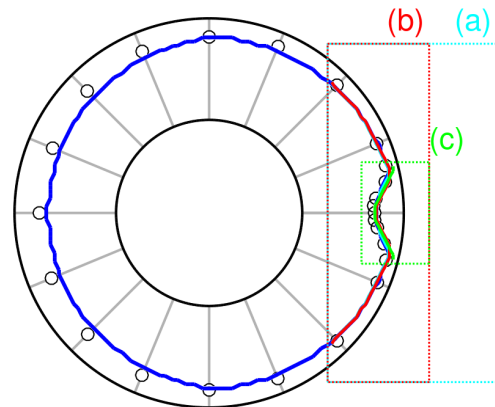
439 In view of sensitivity to the grid size, Fig. 10 shows the run-up limits for the reference scenario  
440 with  $\Delta x = \Delta y = 5$  cm, as well as the solutions of the model with coarser grid sizes of  $\Delta x = \Delta y = 10$  cm  
441 and  $\Delta x = \Delta y = 20$  cm, respectively. The reference mesh size of 5 cm returns the closest agreement  
442 overall with the run-up data - particularly at the lee side of the island. Nevertheless, a numerical  
443 domain with four times fewer cells, i.e., uniform 10 cm grid spacing, still provides a decent estimate  
444 of the run-up, albeit with less precision at the lee side. It is not really surprising that a grid size of  
445  $\Delta x = \Delta y = 20$  cm is too coarse to represent the details of the run-up outline, and virtually no run-up is  
446 recorded in the lee of the island.

447 Careful examination of the temporal evolution of the wave field at  $\Delta x = \Delta y = 5$  cm resolution  
448 shows that the colliding waves in the back of the island locally and momentarily augment the water  
449 level, but then pass through each other and continue the refraction/diffraction process. The locally  
450 high run-up in the back of the island results to a great extent from the two waves that shoal and spill  
451 up on either flank of the leeward side. It often goes unnoticed that the steepened refracted waves  
452 then meet head-on over the leeward topography, i.e. the initially dry beach, from where a substantial  
453 portion of maximum run-up and inundation originates. For a relatively steep slope, this wrapping  
454 process requires rather fine resolution to properly account for the flooding process, and insufficient  
455 grid cells over the beach can lead to an under-representation of the run-up.



— Single grid,  $\Delta x = \Delta y = 20$  cm  
 — Single grid,  $\Delta x = \Delta y = 10$  cm  
 — Single grid,  $\Delta x = \Delta y = 5$  cm

**Figure 10.** Grid size sensitivity of maximum run-up outlines for the test with  $A/h = 0.096$  of Briggs *et al.* (1995). Black dots denote experimental data, solid lines represent results from the present model.



— Single grid,  $\Delta x = \Delta y = 5$  cm  
 — Nested grid (a),  $\Delta x = \Delta y = 5$  cm  
 — Nested grid (b),  $\Delta x = \Delta y = 5$  cm  
 — Nested grid (c),  $\Delta x = \Delta y = 5$  cm

**Figure 11.** Maximum run-up outlines for the test with  $A/h = 0.096$  of Briggs *et al.* (1995). Each model run uses a Parent grid with  $\Delta x = \Delta y = 20$  cm resolution and one Child grid of  $\Delta x = \Delta y = 5$  cm. The three individual nested grid set-ups (a), (b), and (c) and their corresponding maximum run-up limits are color-coded and denoted by the dashed rectangle and the solid lines within.

### Sensitivity to grid nesting:

It is understood that any reduction in the total cell count will reduce the computational load. A nested grid approach caters to lowering the computational effort without compromising too much on the quality of the results. A question of practical interest is whether the overall wave transformation around the island could potentially be computed over a coarse grid, from which information is fed into a nested inner grid of higher resolution that is placed only over a local area of interest. Fig. 10 demonstrates that a grid resolution of 5 cm is an adequate choice for the resolution of the wave run-up along the beach of the conical island and that coarser mesh sizes, in particular the 20 cm resolution, are insufficient to resolve most of the run-up.

The solitary input wave has a length of several meters. As shown in the previous benchmark tests, e.g. 3.3, the present model computes long waves with minimal numerical diffusion and hence is expected to handle the general processes of the solitary wave transformation around the island even over a rather coarse mesh. Inspection of the full free surface evolution has shown that even a grid of 20 cm mesh size can account for the overall wave processes in the vicinity of the conical island and that it only fails in computing the detailed run-up.

Fig. 11 shows the results from three nested grid approaches - all with an inner grid of 5 cm resolution placed into an outer grid of 20 cm resolution. The individual inner domains are color-coded and of 2 m by 4 m, 1.2 m by 4 m and 0.8 m by 1.2 m. The additional computational load arising from the inner grid is associated with 3200, 1920, or 384 cells, respectively. It can be seen that the run-up outline in the nested grid (a) denoted by the cyan line in Fig. 11 is nearly identical to the outline of the uniform 5 cm reference grid. This implies that the overall wave processes are sufficiently resolved by the coarse outer grid up to the boundary of the nested grid (a), which subsequently takes care of the detailed wave transformation and run-up processes at the back side of the conical island. The

479 domain size of the nested grid is then reduced behind the island, as illustrated by the red dashed  
480 rectangle. The corresponding run-up limit (red line) remains nearly identical to the run-up outline  
481 from the largest nested grid setup. The run-up at the lee side, therefore, depends only minimally on  
482 the higher resolution in the area behind the island where the wave collision process occurs. The nested  
483 grid extends to a very small area just around the hotspot of run-up, as denoted by the green dashed  
484 rectangle. Surprisingly, the run-up along the center lee side remains qualitatively very similar to the  
485 run-up computed by the larger nested grids.

486 The effect of the nested grid approaches can be seen in Fig. 12 in more detail. Row 1 shows the  
487 free surface evolution over the 5 cm uniform reference grid. The corresponding alternate solutions,  
488 denoted by the black dashed rectangles, illustrate the nested grid solutions. As the wave is moving  
489 around the island, the nested grid (a) (second row) picks up its energy and resolves the wrap of the  
490 run-up tongue in detail, though with slightly less steepness at the leading edge compared to the  
491 reference solution. The maximum run-up after 9.2 sec in the nested grid is nearly identical to the  
492 uniform reference solution. The third row shows the free surface elevation from the red rectangle  
493 and the run-up limit from Fig. 11. The high-resolution inner grid extends only marginally over the  
494 bathymetry behind the island and mostly covers the topography. The detailed solution of the colliding  
495 waves behind the island is less critical for the maximum run-up than a high-resolution computation of  
496 the two refracted run-up tongues that meet each other over the dry slope. The last row shows that  
497 a representative run-up limit is achievable even by only using an extremely small inner grid of high  
498 resolution at the location where the refracted waves collide over the beach.

499 The long-wave refraction and collision processes do not necessarily require high grid resolution  
500 given that a low-diffusive coarse solution captures the main energy flux. Counter-intuitively, the  
501 locally high run-up of long waves, as illustrated in this example, is often driven by wave processes in  
502 the immediate vicinity of the shoreline and over the beach. Accurate run-up results can potentially be  
503 obtained with locally very small nested grids as long as they cover the entire run-up zone over the  
504 beach. This is particularly true for locations with steep beach slopes.

505 As for the results from Figs. 10 to 12, the computed wave field is symmetric to machine precision  
506 with respect to the horizontal center line at 15 m in the y-direction. This supports the quality of the  
507 numerical results as any instability arising from the interface at the boundary of the nested grids would  
508 have eliminated the perfect symmetry.

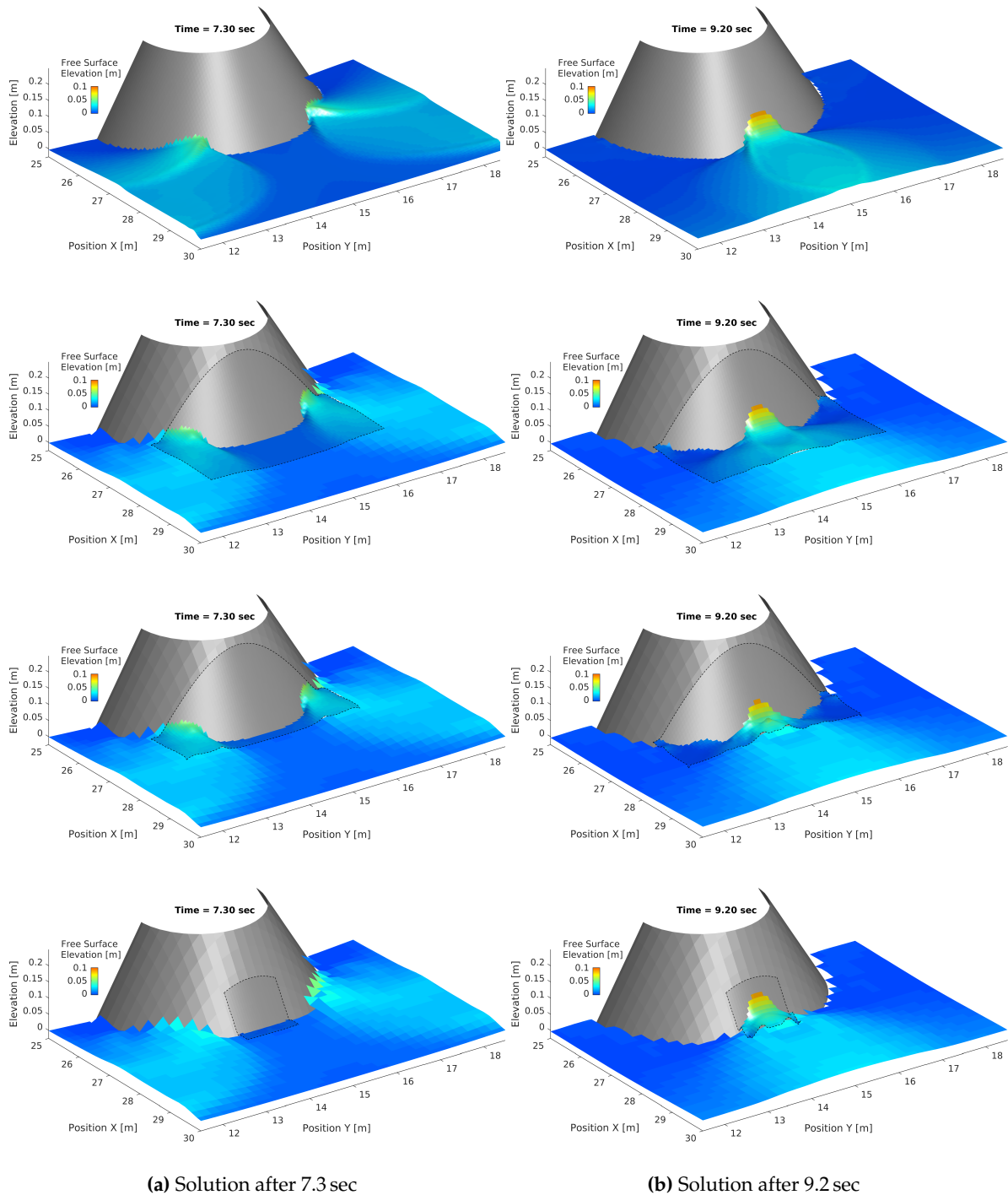


**Figure 12.** Free surface elevation at lee side of conical island computed over the single reference grid of  $\Delta x = \Delta y = 5$  cm (first row) and with three separate grid nesting approaches each combining a coarse outer grid of  $\Delta x = \Delta y = 20$  cm mesh size with inner fine grids of  $\Delta x = \Delta y = 5$  cm resolution (2<sup>nd</sup>, 3<sup>rd</sup>, 4<sup>th</sup> row). First column: Refraction/diffraction of solitary wave around flank of conical island. Second column: Maximum run-up from superposition of refracted/diffracted waves. The extent of the nested grid is outlined by the black dashed line in row 2 to 4.

509 *4.2. Long-wave run-up at Monai Valley*

510 The second benchmark is testing the sensitivity of the present model to the mesh size and  
 511 refinement of the solution with a nested grid for the computation of nonlinear wave processes over an

512 irregular terrain that favors extreme run-up. The 1993 Hokkaido Nansei-Oki tsunami is a well-studied  
 513 event thanks to the laboratory experiments conducted by Matsuyama and Tanaka (2001) at the Central  
 514 Research Institute for Electric Power Industry (CRIEPI) in Japan. The down-scaled laboratory test  
 515 examined the extreme run-up of over 30 m at Monai Valley, located between two headlands and  
 516 sheltered by the small Muen Island. The area around Monai Valley was reconstructed with a plywood  
 517 model at 1:400 scale based on bathymetric and topographic data as shown in Fig. 13.

518 A wave gauge near the wavemaker recorded the initial low amplitude N-wave used in the  
 519 present numerical model as boundary input with the free surface elevation interpolated from the  
 520 data according to the model time step. As in the previous test, we first examine the sensitivity of the  
 521 numerical solution to the grid size over a single domain with uniform resolution. Again, the Courant  
 522 number is kept constant at  $Cr = 0.5$ . A Manning coefficient of  $n = 0.012 \text{ sm}^{-1/3}$  accounts for the surface  
 523 roughness of the plywood model (Chaudhry (2007)).

### 524 Sensitivity to grid resolution:

525 Fig. 14 shows the comparison between the computed and recorded data at the wave gauges placed  
 526 in the numerical and experimental setup between Muen Island and Monai Valley. The computed  
 527 results are of similar quality as the solutions from previous studies. The wave regime at the locations  
 528 of the gauges is still reasonably well resolved with a rather coarse mesh. Even with a 10 cm grid size,  
 529 the general shape of the free surface time series is captured, and the overall energy of the wave field  
 530 behind Muen island is accounted for.

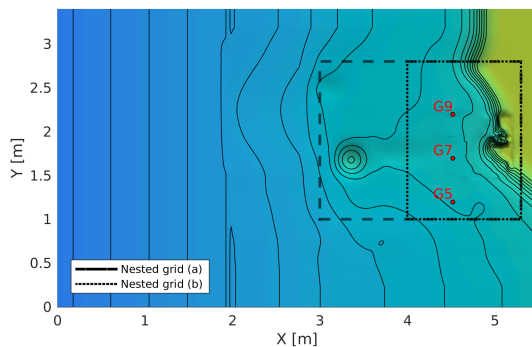


**Figure 13.** Outline of the bathymetry from the 1:400 scaled model used by Matsuyama and Tanaka (2001). The black dashed and dotted lines denotes the boundaries of two individual inner nested grids (a) and (b).

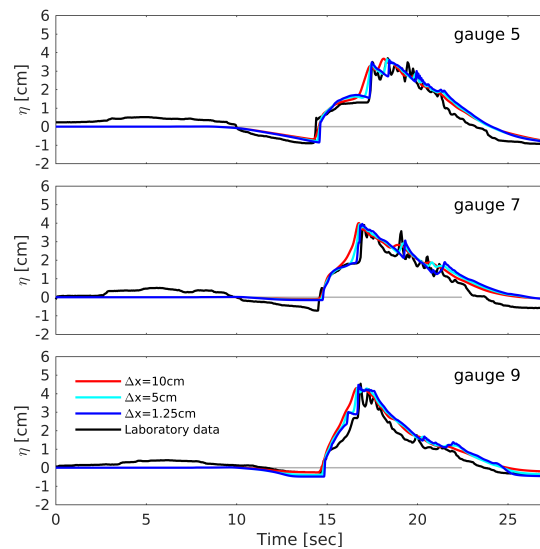


**Figure 14.** Free surface time series at the gauges shown in the left panel from computations over the entire domain with different uniform mesh sizes.

531 Fig. 15(A) illustrates the sensitivity of the computed maximum run-up to different uniform grid  
 532 sizes of 1.25 cm, 2.5 cm, 5 cm, and 10 cm. The local run-up in Monai Valley is more sensitive to the grid  
 533 resolution than the nearshore wave field in front of the beach. Since the terrain is steep and narrow, the  
 534 computations with the present model show that a rather fine grid of 1.25 cm is necessary to obtain a  
 535 proper outline of the run-up envelope. NTHMP (2012) confirms that most previous numerical studies  
 536 utilized a mesh size of  $\Delta x = \Delta y < 1.5 \text{ cm}$  to obtain a consistent definition of the wave run-up in the  
 537 narrow and steep valley. The fine grid of 1.25 cm in the second row of Fig. 16 resolves the details  
 538 of wave refraction and collision in front of the steep cliff, whereas a coarser option of 10 cm resolves  
 539 neither the flow details nor the small-scale flow features over the topography and consequently leads  
 540 to a significant underestimation of the run-up in the Monai Valley.

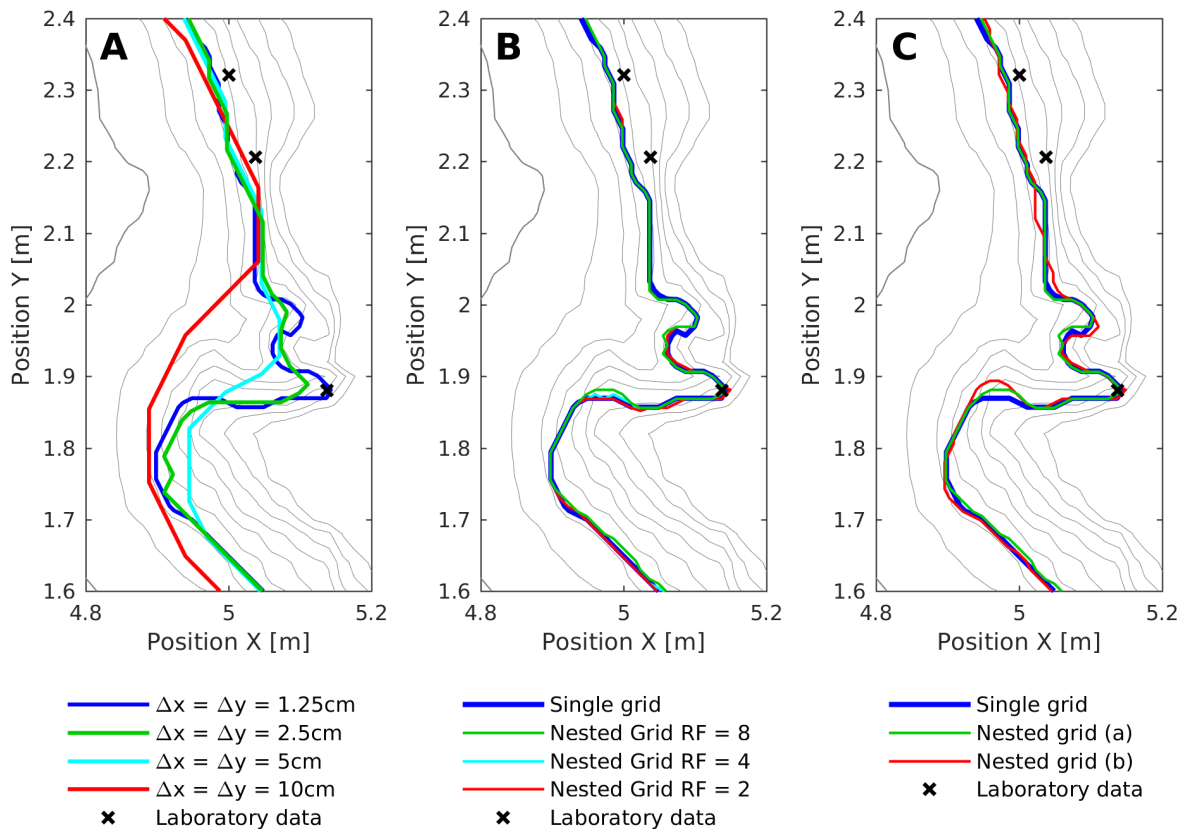


**Figure 15.** Maximum run-up limits around Monai Valley.

Left (A): Uniform grid with different resolutions.

Center (B): Nested grid (a) with 1.25 cm resolution and different Parent grid resolutions of 2.5 cm, 5 cm, and 10 cm leading to refinement factors of  $RF = 2$ ,  $RF = 4$ , and  $RF = 8$

Right (C): Nested grid (a) and (b) with 1.25 cm resolution and Parent grid resolution 10 cm.

#### 541 **Sensitivity to grid nesting:**

542 Similar to the previous benchmark test the question arises whether it is possible to utilize a coarse  
 543 mesh for the overall flow field in combination with a fine nested grid for the detailed run-up in an area  
 544 of interest like Monai Valley. Knowing that the run-up over terrain with irregular and steep slopes  
 545 requires small grid sizes, we utilize a 1.25 cm nested grid (a) inside a Parent grid as outlined in Fig. 13.  
 546 The inner nested grid starts offshore of Muen island, similar to what Yamazaki *et al.* (2011) have used.  
 547 The Parent grid is of 5.5 m by 3.4 m size. It contains only 1870 cells with a 10 cm resolution. The two  
 548 nested grid options (a) and (b) have dimensions of 2.3 m by 1.8 m and 1.3 m by 2.3 m and consequently  
 549 add 26,496 or 14,976 grid cells, respectively, to the computation. Hence, the two nested grid options  
 550 reduce the total cell count by 76% and 86% in comparison to a single grid of uniform 1.25 cm resolution  
 551 with 119,680 cells.

552 The sensitivity of the results with respect to the refinement factor is analyzed by increasing the  
 553 Parent grid resolution by factors of 2, 4, and 8 with respect to the nested grid. Consequently, the  
 554 individual run-up limits of Fig. 15(B) refer to the results from a 1.25 cm nested grid in combination  
 555 with different Parent grids of 2.5 cm, 5 cm, and 10 cm. The refinement factor hardly influences the  
 556 run-up limit with a nested grid domain that covers most of the nearshore area (dashed line of the  
 557 domain (a) in Fig. 13). Again, a basic requirement for the utilization of a coarse Parent grid is a low  
 558 diffusivity of the numerical scheme. It is understood that the interpolation in the nesting process  
 559 between the individual grids can lead to small discrepancies in comparison to a uniform grid with

560 high resolution. This can be seen in Fig. 15. The grid nesting strategy should therefore always be seen  
561 as method to primarily reduce the computational load by still retaining an acceptable quality of the  
562 solution.

563 It is finally shown how the computed results are sensitive to the nested domain size. This is  
564 analyzed through reduction of the area covered by the nested grid (see dotted line (b) in Fig. 13).  
565 The resolutions of the Parent and Child grid are identical to the setup with nested grid (a). The two  
566 scenarios only differ in the domain size of the nested grids. Fig. 15(C) highlights that the run-up limit  
567 from the two scenarios varies only at some locations. Though the flow details of the overtopping and  
568 refraction processes around Muen island are resolved in detail with a fine grid as shown in rows two  
569 and three of Fig. 16, they do not have a substantial influence on the run-up. It is sufficient that the  
570 outer grid resolves the overall wave energy and the inner grid accounts for the run-up process.



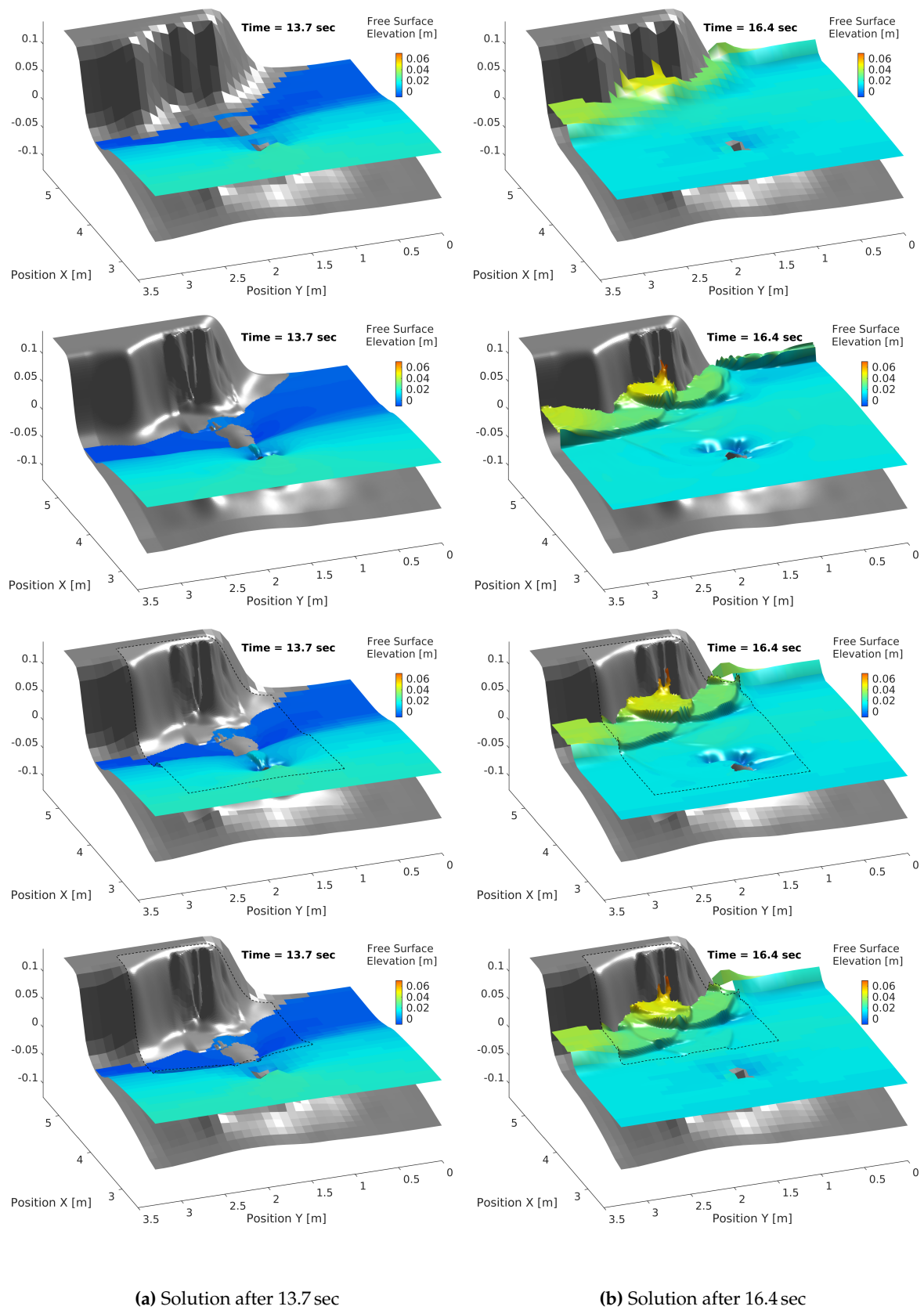


**Figure 16.** Free surface elevation in front of Monai Valley with single Parent grid of  $\Delta x = \Delta y = 10$  cm (first row) and  $\Delta x = \Delta y = 1.25$  cm (second row) mesh size. Results from embedded nested Child grids (a) and (b) of  $\Delta x = \Delta y = 1.25$  cm in a Parent grid of  $\Delta x = \Delta y = 10$  cm are shown in the second row and third row. The extent of the respective Child grid is outlined by the black dashed lines. First column: Drawdown from leading depression of N-wave and approaching wave crest upstream of Muen island. Second column: Maximum run-up from superposition of refracted and reflected waves.

## 571 5. Conclusions and Perspectives

572 We have shown the performance of a newly developed model for long-wave run-up with respect  
573 to standard analytical solutions and laboratory experiments. The model was demonstrated to be  
574 shock-capturing, well-balanced, and water-depth positivity preserving, which are crucial properties  
575 for the correct estimation of long-wave-driven run-up. The model was proven to be stable and efficient  
576 in dealing with wet/dry transitions without the need for computationally expensive treatment of  
577 the moving boundary. The numerical scheme is based on a Finite-Volume staggered approximation  
578 with second-order accuracy in space and time. The accuracy in time arises from a combination of the  
579 Runge-Kutta method for the convective acceleration and the Leapfrog method for the surface gradient  
580 and friction terms. Similarly, the spatial accuracy comes from a second-order upwinded advection  
581 along with a second-order central difference scheme for the remaining terms.

582 The model performs consistently for shock-driven problems and compares to established Riemann  
583 solver-based TVD methods. The wet-dry interface is stable and well-defined without the need for  
584 additional treatment of the moving boundary. The model contains a two-way grid nesting scheme  
585 that allows for local refinement of the solution. The implementation has been verified and proven to  
586 be accurate and stable for moving boundaries and was shown to be applicable to long-wave run-up  
587 problems.

588 The performance and sensitivity of long-wave run-up was then investigated in dependence of  
589 the nested grid's domain size and the level of its refinement. Two standard benchmark tests from the  
590 tsunami community were chosen for the investigation. Though there are no universal rules for the size,  
591 position, and refinement factor of nested grids, our results from the two benchmark tests reveal that  
592 computations of high quality can be achieved with small nested grids placed strategically at a location  
593 of interest such as in areas where locally high run-up occurs. The refinement factor was found to have  
594 only small influence on the run-up limit, if the solution in the Parent grid is representative of the wave  
595 envelope and the grid nesting method accounts for the correct exchange of the total wave energy flux.

596 Further, it was demonstrated that it is possible to place a nested grid rather close to the initial  
597 still-water level as long as the long-wave flow regime prevails across nested grid's offshore boundary.  
598 Long-wave run-up is often more subject to the resolution of the local topography than it is influenced  
599 by the detailed wave processes over the bathymetry. This is line with commonly used empirical run-up  
600 formulae for swell waves where the maximum run-up envelope is controlled by the overall wave  
601 energy and the slope.

602 The quality of the computed results encourages to expand the development of the model with  
603 respect to frequency dispersion. This will allow for a further investigation of how grid nesting  
604 can affect the run-up from swell waves. In the same context, the model can be optimized through  
605 implementation of massive parallelization techniques commonly used to reduce the computation  
606 time associated with large flow problems. It is evident that a low overall cell count reduces the  
607 model's computation time and that the insights gained from the present study can be used to efficiently  
608 decrease the computational load for computations of long waves by retaining accuracy and quality of  
609 the solutions.

## 610 Statements and Declarations

611 The authors acknowledge financial support from the I-SITE program Energy & Environment Solutions  
612 (E2S), the Communauté d'Agglomération Pays Basque (CAPB), and the Communauté Région Nouvelle  
613 Aquitaine (CRNA) for the chair position HPC-Waves. Additional support comes from the European  
614 Union's Horizon 2020 research and innovation programme under grant agreement No 883553.

615 The authors declare no conflict of interest. The funding agencies had no role in the design of the study;  
616 in the collection, analyses, or interpretation of data; in the writing of the manuscript; or in the decision  
617 to publish the results.

## 618 Author Contributions

619 Conceptualization: [Fatima-Zahra Mihami, Volker Roeber];  
 620 Methodology: [Fatima-Zahra Mihami, Volker Roeber];  
 621 Software: [Fatima-Zahra Mihami];  
 622 Formal analysis: [Fatima-Zahra Mihami];  
 623 Validation: [Fatima-Zahra Mihami, Volker Roeber];  
 624 Visualization: [Fatima-Zahra Mihami, Volker Roeber];  
 625 Writing – original draft: [Fatima-Zahra Mihami, Volker Roeber];  
 626 Writing – review & editing: [Fatima-Zahra Mihami, Volker Roeber, Denis Morichon];  
 627 Project administration: [Volker Roeber];  
 628 Funding acquisition: [Volker Roeber];  
 629 Supervision: [Volker Roeber, Denis Morichon].

## 630 Data availability

631 The routines for replication of the numerical results can be provided upon reasonable request.

## 632 References

- 633 Liu, P.L.F.; Synolakis, C.E.; Yeh, H.H. Report on the international workshop on long-wave run-up. *Journal*  
 634 *of Fluid Mechanics* **1991**, *229*, 675–688.
- 635 Carrier, G.F.; Greenspan, H.P. Water waves of finite amplitude on a sloping beach. *Journal of Fluid Mechanics*  
 636 **1958**, *4*, 97–109.
- 637 Synolakis, C.E. The runup of solitary waves. *Journal of Fluid Mechanics* **1987**, *185*, 523–545.
- 638 Thacker, W.C. Some exact solutions to the nonlinear shallow-water wave equations. *Journal of Fluid*  
 639 *Mechanics* **1981**, *107*, 499–508.
- 640 Mayer, R.; Kriebel, D. Wave runup on composite-slope and concave beaches. In *Coastal Engineering 1994;*  
 641 *1995*; pp. 2325–2339.
- 642 Hall, J.V.; Watts, G.M.; others. Laboratory investigation of the vertical rise of solitary waves on impermeable  
 643 slopes. *ARMY COASTAL ENGINEERING RESEARCH CENTER WASHINGTON DC* **1953**.
- 644 Briggs, M.J.; Synolakis, C.E.; Harkins, G.S.; Green, D.R. Laboratory experiments of tsunami runup on a  
 645 circular island. *Pure and applied geophysics* **1995**, *144*, 569–593.
- 646 Briggs, M.J.; Synolakis, C.E.; Kanoglu, U.; Green, D.R. Runup of solitary waves on a vertical wall. Long  
 647 Wave Runup Models: Proc., Int. Workshop, 1996, pp. 375–383.
- 648 Liu, P.L.F.; Woo, S.B.; Cho, Y.S. Computer programs for tsunami propagation and inundation. *Cornell*  
 649 *University* **1998**, *25*.
- 650 Titov, V.V.; Synolakis, C.E. Modeling of breaking and nonbreaking long-wave evolution and runup using  
 651 VTCS-2. *Journal of Waterway, Port, Coastal, and Ocean Engineering* **1995**, *121*, 308–316.
- 652 Brocchini, M.; Dodd, N. Nonlinear shallow water equation modeling for coastal engineering. *Journal of*  
 653 *waterway, port, coastal, and ocean engineering* **2008**, *134*, 104–120.
- 654 Titov, V.; Kânoğlu, U.; Synolakis, C. Development of MOST for real-time tsunami forecasting. PhD thesis,  
 655 American Society of Civil Engineers, 2016.
- 656 George, D.L.; LeVeque, R.J. Finite volume methods and adaptive refinement for global tsunami propagation  
 657 and local inundation. *Science of Tsunami Hazards* **2006**.
- 658 Hervouet, J.M. *Hydrodynamics of free surface flows: modelling with the finite element method*; Vol. 360, Wiley  
 659 Online Library, 2007.
- 660 Wei, Z.; Dalrymple, R.A.; Hérault, A.; Bilotta, G.; Rustico, E.; Yeh, H. SPH modeling of dynamic impact of  
 661 tsunami bore on bridge piers. *Coastal Engineering* **2015**, *104*, 26–42.
- 662 Arakawa, A.; Lamb, V.R. A potential enstrophy and energy conserving scheme for the shallow water  
 663 equations. *Monthly Weather Review* **1981**, *109*, 18–36.
- 664 Imamura, F. Tsunami Numerical Simulation with the Staggered Leap-frog Scheme (Numerical code of  
 665 TUNAMI-N1), School of Civil Engineering, Asian Inst. *Tech. and Disaster Control Research Center, Tohoku*  
 666 *University* **1989**.

- 667 Wang, X. User manual for COMCOT version 1.7 (first draft). *Cornel University* **2009**, 65.
- 668 Shuto, N.; Goto, T. Numerical simulation of tsunami run-up. *Coastal Engineering in Japan* **1978**, *21*, 13–20.
- 669 Titov, V.V.; Synolakis, C.E. Numerical modeling of tidal wave runup. *Journal of Waterway, Port, Coastal, and*  
670 *Ocean Engineering* **1998**, *124*, 157–171.
- 671 Liu, P.L.F.; Cho, Y.S.; Briggs, M.J.; Kanoglu, U.; Synolakis, C.E. Runup of solitary waves on a circular island.  
672 *Journal of Fluid Mechanics* **1995**, *302*, 259–285.
- 673 Wei, Y.; Mao, X.Z.; Cheung, K.F. Well-balanced finite-volume model for long-wave runup. *Journal of*  
674 *Waterway, Port, Coastal, and Ocean Engineering* **2006**, *132*, 114–124.
- 675 Olabarrieta, M.; Medina, R.; Gonzalez, M.; Otero, L. C3: A finite volume-finite difference hybrid model for  
676 tsunami propagation and runup. *Computers & geosciences* **2011**, *37*, 1003–1014.
- 677 Godunov, S. Different methods for shock waves. *Moscow State University* **1954**.
- 678 Roe, P.L. Characteristic-based schemes for the Euler equations. *Annual review of fluid mechanics* **1986**,  
679 *18*, 337–365.
- 680 Berger, M.J.; George, D.L.; LeVeque, R.J.; Mandli, K.T. The GeoClaw software for depth-averaged flows  
681 with adaptive refinement. *Advances in Water Resources* **2011**, *34*, 1195–1206.
- 682 Macías, J.; Castro, M.J.; Ortega, S.; Escalante, C.; González-Vida, J.M. Performance benchmarking of  
683 tsunami-HySEA model for NTHMP's inundation mapping activities. *Pure and Applied Geophysics* **2017**,  
684 *174*, 3147–3183.
- 685 Dutykh, D.; Poncet, R.; Dias, F. The VOLNA code for the numerical modeling of tsunami waves: Generation,  
686 propagation and inundation. *European Journal of Mechanics-B/Fluids* **2011**, *30*, 598–615.
- 687 Yuan, Y.; Shi, F.; Kirby, J.T.; Yu, F. FUNWAVE-GPU: Multiple-GPU Acceleration of a Boussinesq-Type Wave  
688 Model. *Journal of Advances in Modeling Earth Systems* **2020**, *12*, e2019MS001957.
- 689 Roe, P.L. Approximate Riemann solvers, parameter vectors, and difference schemes. *Journal of computational*  
690 *physics* **1997**, *135*, 250–258.
- 691 Harten, A.; Lax, P.D.; Leer, B.v. On upstream differencing and Godunov-type schemes for hyperbolic  
692 conservation laws. *SIAM review* **1983**, *25*, 35–61.
- 693 Toro, E. A weighted average flux method for hyperbolic conservation laws. *Proceedings of the Royal Society*  
694 *of London. A. Mathematical and Physical Sciences* **1989**, *423*, 401–418.
- 695 Zijlema, M. The role of the Rankine-Hugoniot relations in staggered finite difference schemes for the  
696 shallow water equations. *Computers & Fluids* **2019**, *192*, 104274.
- 697 LeVeque, R.J. Balancing source terms and flux gradients in high-resolution Godunov methods: the  
698 quasi-steady wave-propagation algorithm. *Journal of computational physics* **1998**, *146*, 346–365.
- 699 Zhou, J.G.; Causon, D.M.; Mingham, C.G.; Ingram, D.M. The surface gradient method for the treatment of  
700 source terms in the shallow-water equations. *Journal of Computational physics* **2001**, *168*, 1–25.
- 701 Brufau, P.; Vázquez-Cendón, M.; García-Navarro, P. A numerical model for the flooding and drying of  
702 irregular domains. *International Journal for Numerical Methods in Fluids* **2002**, *39*, 247–275.
- 703 Toro, E.F. *Shock-capturing methods for free-surface shallow flows*; Vol. 868, Wiley New York, 2001.
- 704 Audusse, E.; Chalons, C.; Ung, P. A simple well-balanced and positive numerical scheme for the  
705 shallow-water system. *Communications in Mathematical Sciences* **2015**, *13*, 1317–1332.
- 706 Dodd, N. Numerical model of wave run-up, overtopping, and regeneration. *Journal of Waterway, Port,*  
707 *Coastal, and Ocean Engineering* **1998**, *124*, 73–81.
- 708 Audusse, E.; Bouchut, F.; Bristeau, M.O.; Klein, R.; Perthame, B.t. A fast and stable well-balanced scheme  
709 with hydrostatic reconstruction for shallow water flows. *SIAM Journal on Scientific Computing* **2004**,  
710 *25*, 2050–2065.
- 711 Shi, F.; Kirby, J.T.; Harris, J.C.; Geiman, J.D.; Grilli, S.T. A high-order adaptive time-stepping TVD solver  
712 for Boussinesq modeling of breaking waves and coastal inundation. *Ocean Modelling* **2012**, *43 – 44*, 36–51.  
713 doi:10.1016/j.ocemod.2011.12.004.
- 714 Kim, D.H.; Lynett, P.J.; Socolofsky, S.A. A depth-integrated model for weakly dispersive, turbulent, and  
715 rotational fluid flows. *Ocean Modelling* **2009**, *27*, 198–214.
- 716 Roeber, V.; Cheung, K.F. Boussinesq-type model for energetic breaking waves in fringing reef environments.  
717 *Coastal Engineering* **2012**, *70*, 1–20.
- 718 Zhou, J.; Stansby, P. 2D shallow water flow model for the hydraulic jump. *International Journal for Numerical*  
719 *Methods in Fluids* **1999**, *29*, 375–387.

- 720 Stelling, G.S.; Duijnmeijer, S.A. A staggered conservative scheme for every Froude number in rapidly  
721 varied shallow water flows. *International journal for numerical methods in fluids* **2003**, *43*, 1329–1354.
- 722 Madsen, P.A.; Simonsen, H.J.; Pan, C.H. Numerical simulation of tidal bores and hydraulic jumps. *Coastal*  
723 *Engineering* **2005**, *52*, 409–433.
- 724 Doyen, D.; Gunawan, P.H. An explicit staggered finite volume scheme for the shallow water equations. In  
725 *Finite Volumes for Complex Applications VII-Methods and Theoretical Aspects*; Springer, 2014; pp. 227–235.
- 726 Yamazaki, Y.; Kowalik, Z.; Cheung, K.F. Depth-integrated, non-hydrostatic model for wave breaking and  
727 run-up. *International journal for numerical methods in fluids* **2009**, *61*, 473–497.
- 728 Zijlema, M.; Stelling, G.; Smit, P. SWASH: An operational public domain code for simulating wave fields  
729 and rapidly varied flows in coastal waters. *Coastal Engineering* **2011**, *58*, 992–1012.
- 730 Yamazaki, Y.; Cheung, K.F.; Kowalik, Z.; Lay, T.; Pawlak, G. Neowave. Proceedings and results of the  
731 2011 NTHMP model benchmarking workshop, Boulder: US Department of Commerce/NOAA/NTHMP  
732 (NOAA Special Report), 2012, pp. 239–302.
- 733 Roelvink, D.; McCall, R.; Mehvar, S.; Nederhoff, K.; Dastgheib, A. Improving predictions of swash dynamics  
734 in XBeach: The role of groupiness and incident-band runup. *Coastal Engineering* **2018**, *134*, 103–123.
- 735 Yamazaki, Y.; Cheung, K.F.; Kowalik, Z. Depth-integrated, non-hydrostatic model with grid nesting for  
736 tsunami generation, propagation, and run-up. *International Journal for Numerical Methods in Fluids* **2011**,  
737 *67*, 2081–2107.
- 738 Sætra, M.L.; Brodtkorb, A.R.; Lie, K.A. Efficient GPU-implementation of adaptive mesh refinement for the  
739 shallow-water equations. *Journal of Scientific Computing* **2015**, *63*, 23–48.
- 740 Donat, R.; Martí, M.C.; Martínez-Gavara, A.; Mulet, P. Well-balanced adaptive mesh refinement for shallow  
741 water flows. *Journal of Computational Physics* **2014**, *257*, 937–953.
- 742 Liang, Q. A structured but non-uniform Cartesian grid-based model for the shallow water equations.  
743 *International Journal for Numerical Methods in Fluids* **2011**, *66*, 537–554.
- 744 Debreu, L.; Blayo, E. Two-way embedding algorithms: a review. *Ocean Dynamics* **2008**, *58*, 415–428.
- 745 Gottlieb, S.; Shu, C.W.; Tadmor, E. Strong stability-preserving high-order time discretization methods.  
746 *SIAM review* **2001**, *43*, 89–112.
- 747 Gunawan, H.P. Numerical simulation of shallow water equations and related models. PhD thesis, Paris  
748 Est, 2015.
- 749 Liu, P.L.F.; Cho, Y.S.; Yoon, S.; Seo, S. Numerical simulations of the 1960 Chilean tsunami propagation and  
750 inundation at Hilo, Hawaii. In *Tsunami: Progress in prediction, disaster prevention and warning*; Springer, 1995;  
751 pp. 99–115.
- 752 Herzfeld, M.; Rizwi, F. A two-way nesting framework for ocean models. *Environmental Modelling &*  
753 *Software* **2019**, *117*, 200–213.
- 754 Phillips, N.A.; Shukla, J. On the strategy of combining coarse and fine grid meshes in numerical weather  
755 prediction. *Journal of Applied Meteorology and Climatology* **1973**, *12*, 763–770.
- 756 Zhang, D.L.; Chang, H.R.; Seaman, N.L.; Warner, T.T.; Fritsch, J.M. A two-way interactive nesting procedure  
757 with variable terrain resolution. *Monthly Weather Review* **1986**, *114*, 1330–1339.
- 758 Oey, L.Y.; Chen, P. A nested-grid ocean model: With application to the simulation of meanders and eddies  
759 in the Norwegian Coastal Current. *Journal of Geophysical Research: Oceans* **1992**, *97*, 20063–20086.
- 760 Van Leer, B. Towards the ultimate conservative difference scheme. V. A second-order sequel to Godunov's  
761 method. *Journal of computational Physics* **1979**, *32*, 101–136.
- 762 Stoker, J. *Water Waves. The Mathematical Theory with Applications*, Interscience Publ. Inc., New York  
763 **1957**.
- 764 Dressler, R.F. *Hydraulic resistance effect upon the dam-break functions*; Vol. 49, National Bureau of Standards  
765 Washington, DC, 1952.
- 766 Whitham, G.B. The effects of hydraulic resistance in the dam-break problem. *Proceedings of the Royal Society*  
767 *of London. Series A. Mathematical and Physical Sciences* **1955**, *227*, 399–407.
- 768 Chanson, H. Application of the method of characteristics to the dam break wave problem. *Journal of*  
769 *Hydraulic Research* **2009**, *47*, 41–49.
- 770 Delestre, O.; Lucas, C.; Ksinant, P.A.; Darboux, F.; Laguerre, C.; Vo, T.N.T.; James, F.; Cordier, S. SWASHES:  
771 a compilation of shallow water analytic solutions for hydraulic and environmental studies. *International*  
772 *Journal for Numerical Methods in Fluids* **2013**, *72*, 269–300.

- 773 NTHMP. National Tsunami Hazard Mitigation Program. *Proceedings and Results of the 2011 NTHMP Model*  
774 *Benchmarking Workshop, Boulder: U.S. Department of Commerce/NOAA/NTHMP, (NOAA Special Report) 2012,*  
775 *pp. 1–436.*
- 776 Chaudhry, M.H. *Open-channel flow*; Springer Science & Business Media, 2007.
- 777 Matsuyama, M.; Tanaka, H. An experimental study of the highest run-up height in the 1993 Hokkaido  
778 Nansei-oki earthquake tsunami. National Tsunami Hazard Mitigation Program Review and International  
779 Tsunami Symposium (ITS), 2001, pp. 879–889.